Susorney, H. C. M., Barnouin, O. S., Ernst, C. M., & Johnson, C. L. (2016). Morphometry of impact craters on Mercury from MESSENGER altimetry and imaging. *Icarus*, *271*, 180-193. https://doi.org/10.1016/j.icarus.2016.01.022

Morphometry of Impact Craters on Mercury from MESSENGER Altimetry and Imaging

Hannah C. M. Susorney[1], Olivier S. Barnouin[2], Carolyn M. Ernst[2], Catherine L. Johnson[3,4]

[1]Department of Earth and Planetary Sciences, The Johns Hopkins University, Baltimore, MD 21218, USA.

[2]The Johns Hopkins University Applied Physics Laboratory, Laurel, MD 20723, USA.

[3]Department of Earth, Ocean and Atmospheric Sciences, University of British Columbia, Vancouver, BC, V6T 1Z4, Canada

[4]Planetary Science Institute, Tucson, AZ 85719, USA

Submitted to Icarus: June 11, 2015

Revisions submitted to Icarus: November 9, 2015

Accepted:

Corresponding author: H. C. M. Susorney, Department of Earth and Planetary Sciences, The Johns Hopkins University, 3400 N. Charles Street, Baltimore, MD 21218, USA.

Phone: (410) 516-7135. E-mail address: hsusorn1@jhu.edu

Abstract

Data acquired by the Mercury Laser Altimeter and the Mercury Dual Imaging System on the MESSENGER spacecraft in orbit about Mercury provide a means to measure the geometry of many of the impact craters in Mercury's northern hemisphere in detail for the first time. The combination of topographic and imaging data permit a systematic evaluation of impact crater morphometry on Mercury, a new calculation of the diameter D_t at which craters transition with increasing diameter from simple to complex forms, and an exploration of the role of target properties and impact velocity on final crater size and shape. Measurements of impact crater depth on Mercury confirm results from previous studies, with the exception that the depths of large complex craters are typically shallower at a given diameter than reported from Mariner 10 data. Secondary craters on Mercury are generally shallower than primary craters of the same diameter. No significant differences are observed between the depths of craters within heavily cratered terrain and those of craters within smooth plains. The morphological attributes of craters that reflect the transition from simple to complex craters do not appear at the same diameter; instead flat floors first appear with increasing diameter in craters at the smallest diameters, followed with increasing diameter by reduced crater depth and rim height, and then collapse and terracing of crater walls. Differences reported by others in D_t between Mercury and Mars (despite the similar surface gravitational acceleration on the two bodies) are confirmed in this study. The variations in D_t between Mercury and Mars cannot be adequately attributed to differences in either surface properties or mean projectile velocity.

Keywords: Mercury, surface; Impact processes; Cratering

Highlights:

1. The geometry of 331 primary impact craters on Mercury has been measured.
2. Fresh craters of a given diameter on Mercury may vary in depth.
3. Complex craters on Mercury have diameters greater than 11.7 ± 1.2 km.
4. This transition diameter is larger on Mercury than on Mars.
5. Depths of simple craters on Mercury and Mars are not statistically different.

1. Introduction

Multiple factors control the geometry of impact craters, including the surface gravitational acceleration on the target body (e.g., Pike, 1980) and the physical characteristics of the target and projectile (e.g., Fulmer and Roberts, 1963; Gault and Wedekind, 1978; Gault et al., 1968; Schultz, 1988; Holsapple, 1993; Hermalyn and Schultz, 2011). From the morphometry of impact craters, inferences can be made about the respective roles of the physical properties of the target (e.g., Kalynn et al., 2013) and the projectile population (e.g., Strom et al., 2005). Documenting crater morphometry on Mercury and comparing results with those from Mars are of particular interest because of the similar surface gravitational acceleration on those two planets. However, Mars and Mercury are characterized by different impactor velocities (Le Feuvre and Wieczorek, 2008; Marchi et al., 2012) and surface properties (e.g., Pike, 1980).

The diameter D_t at which craters transition with increasing diameter from simple (bowl-shaped) to complex (flat-floored with terraced walls and often with central peaks) forms scales with the inverse of the surface gravitational acceleration of the target body (Pike, 1980). Despite the similar surface gravitational acceleration (about 3.7 m/s^2) on Mercury and Mars, however, early studies indicated that the two bodies have somewhat different transition diameters of 10.4 ± 4 km and 5.8 ± 2 km, respectively (Pike, 1980, 1988), although the uncertainties in those values overlap at the one-standard-deviation level.

Recent studies of D_t on Mercury conducted with data from the MErcury Surface, Space ENvironment, GEochemistry, and Ranging (MESSENGER) spacecraft have yielded different values. A study combining shadow measurements made from Mercury Dual Imaging System (MDIS) images and Mercury Laser Altimeter (MLA) data acquired during MESSENGER's first two Mercury flybys (M1 and M2, respectively; MESSENGER's third flyby is denoted M3)

reported a D_t value of ~12 km (no uncertainty reported) (Barnouin et al., 2012). A determination of D_t with MLA data from the first year of MESSENGER orbital operations yielded a value of ~8 km (no uncertainty reported) (Talpe et al., 2012). These studies used only the intersection of power laws fit to determinations of depth versus diameter for simple and complex craters to calculate D_t. Neither study included a more complete assessment of the attributes that mark the onset of complex crater morphology (e.g., Pike, 1980, 1988). Possible reasons for the difference in D_t between the two studies may result from differences in the crater populations studied (e.g., freshness criteria, whether secondary craters may have been included, and the locations of the craters used in the study). The erosional degradation of craters over time is known to decrease crater depth (Wood et al., 1977), and secondary craters tend to be shallower than primary craters (e.g., Schultz and Gault, 1985). The incorporation of degraded craters or secondary craters into a D_t calculation may result in a smaller value of D_t, as the inclusion of these shallower craters can change the resulting power-law fits (see section 3.3). Freshness criteria used by Talpe et al. (2012) were not provided, and those workers did not specify whether only primary craters were used. Barnouin et al. (2012) measured only primary craters and assessed crater degradation state with the system of Trask (1971). Further, the locations of the craters used in the two studies were different. Talpe et al. (2012) focused on polar craters, whereas Barnouin et al. (2012) measured craters in near-equatorial regions, so the respective crater populations may have sampled different target properties.

A study of data from the Mars Orbiter Laser Altimeter (MOLA) on the Mars Global Surveyor spacecraft yielded a D_t value for Mars of 8.0 ± 0.5 km (Garvin and Frawley, 1998), nominally larger than that found earlier by Pike (1980). The former study did not include morphologic indicators or track crater freshness in the determination of D_t, but rather relied only

on the intersection of the power laws fit to the depth-versus-diameter data for the deepest simple and complex craters in the data sets. Robbins and Hynek (2012b) used topography from MOLA and images from the Thermal Emission Imaging System (THEMIS) on the Mars Odyssey spacecraft to determine a D_t value for Mars of 5.6 ± 2.3 km. Robbins and Hynek (2012b) also used morphologic indicators similar to those of Pike (1980) and tracked crater freshness. Studies of D_t value for different regions on Mars have yielded different values. Regions interpreted to have stronger surfaces (e.g., intact crystalline rocks) have a larger D_t value than regions that inferred to be weaker (Boyce et al., 2006; Robbins and Hynek, 2012b).

If the D_t values of Mercury and Mars are resolvably different, then surface gravitational acceleration is not the only factor controlling the transition from simple to complex crater morphology, and projectile and surface properties must be investigated. Understanding the role of gravitational acceleration versus projectile and surface properties is important in interpreting final crater morphometry, in particular when comparing crater morphometry on different bodies. Calculating a new D_t for Mercury (with an associated uncertainty) from altimetry data gathered by the MESSENGER spacecraft permits a direct comparison with calculations of the D_t of Mars from MOLA data (e.g., Robbins and Hynek, 2012b).

The insertion of the MESSENGER spacecraft into orbit about Mercury in March 2011 has provided high-resolution images of the surface from MDIS and topographic measurements from MLA. The combination of the datasets permits a thorough examination of the morphometry of Mercury's impact crater population at both a resolution and degree of spatial coverage not previously available. We have used the classification system of Trask (1971) to identify the freshest primary craters for the calculation of D_t. We have assessed several attributes that mark the onset of complex crater morphology (Pike, 1980, 1988). These procedures permit a direct

comparison of our results with those for Mars (Pike, 1980; Robbins and Hynek, 2012b) as well as an examination of whether the D_t estimate depends on the physical diagnostic used.

In the following sections we give a brief overview of projectile and target properties that may control final crater morphometry, discuss the measurement techniques employed with both the MLA and MDIS datasets to obtain the depth (d), diameter (D), rim height (h), floor diameter (D_f), wall width (w), and central uplift height (r) of craters. We then describe how crater degradation state was determined and target geology identified. We present our results for the variation in d, h, w and r with crater diameter, together with the new value of D_t for Mercury. Finally, we discuss the measurements with a focus on implications for the impact cratering process on Mercury and Mars, Mercury's surface properties, and the role of the projectile velocity on final crater morphometry.

2. Impact conditions that influence crater morphometry

The formation of impact craters and the subsequent final crater morphometry are controlled by a body's surface gravitational acceleration (Pike, 1980) and to a lesser extent by the properties of the projectile and target (e.g., Holsapple, 1993). Here we review how target and projectile properties have been observed to modify final crater morphometry. These observations are used below to understand the factors that may be affecting the possible difference in the D_t values for Mercury and Mars and variations in crater morphometry across Mercury itself.

Target properties that have a demonstrated effect on crater size and shape (and thus the D_t value) include strength (which is in turn determined by the history of local fracturing and any mechanical layering) and porosity. Investigations of the role of target strength during simple crater formation (Fulmer and Roberts, 1963; Shoemaker, 1963; Gault et al., 1968; Cintala et al.,

1977a,b; Holsapple, 1993; Barnouin-Jha et al., 2007) have shown that an increase in target strength can restrict the amount of collapse during the temporal transition from transient to final crater geometry. The result is that deeper simple craters form in stronger targets. The effect of target porosity on final crater depth is not well understood, with some workers reporting both shallower and deeper craters in highly porous targets (e.g., Housen and Holsapple, 2003) and others reporting only shallower craters in porous targets (Schultz et al., 2005). The interaction between target porosity and target strength may be the source of the discrepancy among studies.

Recent investigations of the *d/D* ratio on the Moon and Mars indicate that both target strength and porosity influence crater morphometry. On the Moon, complex craters in the highlands are deeper than craters of similar diameter in the maria (Kalynn et al., 2013). Both the greater strength of (and possible layering effects in) mare deposits and the greater porosity of highlands material (an average porosity of 12%; Wieczorek et al., 2013) have been cited as the source of the differences in the final depth of fresh craters of a given diameter (Kalynn et al., 2013). On Mars, target strength has been invoked as the primary factor influencing morphometry of simple craters, but not complex ones. Most investigators of *d/D* for fresh or pristine (see section 5.4 for a further definition of these terms) simple craters (Boyce et al., 2006; Boyce and Garbeil, 2007; Stewart and Valiant, 2006; Robbins and Hynek, 2012a,b) have reported regional differences in the *d/D* ratio of simple craters. Many of these workers invoked target strength (Boyce et al., 2006; Stewart and Valiant, 2006) as the main cause of this difference, suggesting that stronger targets resist collapse (Boyce et al., 2006). Although Stewart and Valiant (2006) suggested that fresh complex craters also vary in *d/D* with terrain type, a more statistical rigorous investigation using a greater number of craters could not confirm this result for complex craters (Robbins and Hynek, 2012b).

Projectile density, velocity, and the impact angle – the angle that the impactor trajectory makes with the surface tangent or horizontal – may contribute to the final shape of observed craters. Experimental investigations of low-density projectiles have demonstrated a reduction in the depths of craters as a result of limited penetration into the target (e.g., Hermalyn and Schultz, 2011). Early investigators suggested that low-density objects might be an important component of the impactor population at the innermost planet given that comet orbits frequently cross Mercury's orbit (Hartmann, 1981; Horedt and Neukum, 1984; Schultz, 1988; Neukum and Ivanov, 1994). A more recent study, however, indicates that the cratering record on Mercury resembles closely those of the Moon and Mars, an observation that is best explained if the cratering record of all three bodies is dominated by impacts from asteroids (Strom et al., 2005). The distribution of projectile densities at Mercury, therefore, is likely to have been similar to those for other planets in the inner solar system.

Unlike projectile density, the distribution of impact velocities on Mercury is very different from those on other inner solar system bodies. Dynamical models indicate that the mean expected velocity of projectiles is 42 km/s on Mercury, compared with only 10 km/s on Mars (Le Feuvre and Wieczorek, 2008; Marchi et al., 2012). Further, these studies have shown that the projectile velocity on Mercury is not only greater on average but also substantially more variable (20–65 km/s) than on Mars (8–12 km/s). Impact cratering experiments have suggested that higher-velocity projectiles produce deeper final (shallower transient) craters (Schultz, 1988; Barnouin et al., 2011). Numerical studies have suggested a more complicated situation, where at some impact velocity, craters cease becoming deeper and either produce the same *d/D* (Jutzi and Michel, 2014) or produce shallower craters (Bray and Schenk, 2015).

Highly oblique impacts (i.e., impact angles less than 15°) are known to produce unusually shallow craters for a given projectile diameter from laboratory studies (e.g., Gault and Wedekind, 1978; Hessen et al., 2007). In studies of highly oblique impact craters on Venus and the Moon, no change in *d/D* was found when depth was measured from a preexisting surface (Herrick and Forsberg-Taylor, 2003), but rim heights were found to vary around the crater. On Mercury (as with other bodies), impacts at low impact angles represent only a small fraction of the total population and are unlikely to be a major contributor to observed crater geometries (Shoemaker, 1962; Le Feuvre and Wieczorek, 2008). Further, highly oblique impacts can be recognized from the crater planform, the asymmetric distribution of ejecta and crater rays (e.g., Gault and Wedekind, 1978), and the interior structure of craters (e.g., Schultz, 1992). In this study, we avoid analyzing any results from craters that possess these oblique impact characteristics.

3. Measurements of crater geometry from MLA and MDIS

The orbital coverage of Mercury's northern hemisphere by both MLA and MDIS permits the assessment of crater degradation state and the measurement of crater geometry at a resolution and accuracy not previously possible. The use of MLA data provides an accurate measure of crater topography (e.g., Barnouin et al., 2012; Talpe et al., 2012) and avoids the ambiguity associated with shadow measurements (see discussion by Pike, 1988). We used individual MLA tracks instead of MLA-derived digital elevation models (DEMs). The use of DEMs can be problematic for measuring the shapes of small (<10 km diameter) craters because of the size of the altimetry footprints (15–100 m) and their along-track spacing (300–800 m, Zuber et al., 2012). In addition, interpolation between MLA tracks at low latitudes is an issue for smaller

craters. For example, the depth for a small crater inferred from a DEM may have been interpolated from tracks across the lower walls of a crater and thus not represent the depth of the crater floor. This scenario can bias estimates of depth for simple craters, as well as d/D (and D_t) values that do not reflect those of the actual crater population. Similar issues have been observed with MOLA-derived DEMs for Mars (e.g., Glaze et al., 2003; Barnouin-Jha et al., 2005; Robbins and Hynek, 2013). In this study, we therefore measured crater geometry directly from co-registered MLA tracks and MDIS images (Fig. 1), allowing the topography viewed in the MLA tracks to be directly correlated with crater morphology seen in the MDIS images. We also restricted our study to craters with $D > 3$ km.

For each crater investigated, we used (when available) three MLA tracks that crossed the crater. This number was found to be sufficient to measure the natural variation in rim height and depth, as well as all other measurements of crater shape. For five craters chosen at random, no differences in the results were obtained for rim crest height or crater depth when using five MLA tracks rather than three. In all cases, the measured results were well within the errors obtained for these measurements when using just three MLA tracks. A similar result was found when measuring small craters on the Moon with just two transects (Stopar et al., 2012). For craters with $D > 20$ km, suitable MLA tracks were located on a monochrome base map of Mercury (250 m pixel scale), which was sufficient for the determination of crater degradation state. Smaller craters required the registration of MLA tracks with individual MDIS images at full resolution (pixel scales as good as a few tens of meters) to best assess the crater morphometry and degradation state. The MLA and MDIS co-registration was excellent (to within one MLA footprint, i.e., 60 μ rad, better than the pointing of MOLA for example), but occasional offsets were noted when the emission angle (measured from vertical) of the MDIS image exceeded 80°.

Therefore we used only those MDIS images with emission angles <80°. Each measurement reported (e.g., *d*, *h*) for a given crater is an average of the results obtained from the three MLA tracks. The total uncertainty attributed to each measurement (with the exception of the central uplift height) was determined by taking the root mean square of the errors associated with each individual measurement (which are described below for each measurement type) and the standard deviation of three individual measurements to calculate a final uncertainty.

The individual MDIS high-resolution images were also used to find MLA tracks that bisected (i.e., passed through the center) of small (D < 20 km) craters. Such a bisection was required to measure accurately the depth of bowl-shaped craters, since MLA tracks that intersected only the sides of simple craters provided inaccurate measures of crater depth. MLA transects were considered suitable for analysis if they bisected the crater and the number of footprints within each crater was greater than five.

For larger complex craters, multiple MLA tracks were often available. In such a situation, MLA transects that intersected the central uplift (peak or peak ring) of the crater were selected first. When fewer than three MLA transects bisected the central uplift, we also used transects that sampled other portions of the crater floor for our estimate of depth. When this occurred, the depth reported for transects that sampled the central uplift and the depth reported for transects that sampled only the crater floor were the same within the uncertainties associated with each measurement. Different observers repeated many of the measurements in this study to check for observational biases; measurements were consistent within the reported uncertainties. Measurements of crater geometrical parameters were stored together with an image of the crater, which permitted each crater (outliers in particular) to be investigated relative to the overall population when assessing factors influencing crater morphometry on Mercury. All

measurements and their associated errors are listed in Table A1 in Appendix 1 for 331 primary impact craters on Mercury.

3.1. Crater geometry measurements

3.1.1. Crater depth and rim height

To measure a crater's depth (*d*) and rim height (*h*), a function was fit to the individual footprints of each MLA transect to remove regional topography. To fit the function, MLA points were selected beyond the edge of a crater's ejecta deposits (carefully avoiding nearby craters, scarps, and ejecta deposits from other nearby craters) to at least three crater radii away from the center of the crater. A second-order polynomial (found to be a better fit to the background topography than a line) was used to remove regional elevation.

The height of the rim crest was measured on both sides of the crater by selecting the highest MLA elevation on the rim crest, when the return was within one MLA footprint of the rim crest. Such an approach yields robust results relative to other efforts (e.g., Robbins and Hynek, 2012b, 2013) for several reasons. First, the MLA instrument measures range by determining the time when the returned pulse first arrives at the detector (it does not measure the time to the peak of the pulse). As a result, MLA measurements are biased on average toward measuring the highest feature in the footprint (i.e., they are more likely to measure a high rim crest). Second, the knowledge of MLA's pointing with respect to MDIS is well understood, to within a few pixels of MDIS narrow-angle camera (NAC) data or about one MLA footprint (~15 m near the poles and ~100 m at the equator). This knowledge means we were able to identify MLA returns at locations very near a crater's rim crest and that the rim height reported is the height of the crest rather than an average over the rim. The resulting value of *h* was calculated as

the difference between the height of the rim crest and that of the pre-existing surface (inferred from regional topography). Natural variations in rim height were captured by the use of three MLA tracks to independently measure *h* and *d*. The value of *d* reported is the average of the difference between the height of the rim crest and the lowest MLA-measured elevation of the crater floor for three MLA tracks (Fig. 1).

3.1.2. Crater diameter and floor diameter

The crater diameter (*D*) was measured by tracing out the rim crest (utilizing the MLA track as an additional guide for capturing the precise location of the rim crest) on an MDIS image projected in simple cylindrical geometry centered over the crater center and finding a best-fit circle using least squares to the traced points. The fits were made after converting the traces into measurements of distance (by recalculating the center from the least squares fit). The floor diameter D_f, defined by the average diameter of the intersection of the flat floor with the crater wall, was measured with the same methodology. The uncertainty of each measured *D* (and D_f) is equal to one standard deviation of the errors in the fit of a circle to the crater's rim outline. The final reported value of *D* (and D_f) for a given crater is the mean of three measurements, each using a different MLA track as an additional guide. The measurement was repeated three times to achieve a best estimate of *D* (and D_f), given the error introduced when hand-tracing a crater rim crest (or floor diameter). Most of the uncertainty in *D* (and D_f) can be attributed to the lack of circularity that naturally occurs in most craters.

3.1.3. Central uplift height

The height r of the central uplift was recorded only for a subset of the craters investigated. The selection of suitable central uplift measurements was achieved through inspection of the location of an MLA track on an MDIS image and the use of shadow length measurements as guides to help identify a representative high point. Only measurements taken from profiles where the MLA track sampled the highest point in the central uplift structure are reported in this study. The value of r was taken as the difference between the highest elevation measurement on the central uplift and the average of the six lowest elevation measurements of the crater floor. The uncertainty in r was calculated from the standard deviation of the difference in the six lowest elevation measurements on the crater floor.

3.1.4. Wall width

The wall width (w) of craters was calculated from the D_f and D values for the crater:

$$w = (D - D_f)/2 \quad (1)$$

The uncertainty in the measurement was calculated by propagation of the uncertainties in D_f and D.

3.2. Crater observations

3.2.1. Classification of crater degradation

The MDIS base map and individual images were used to identify the relative degradation state of each crater analyzed on the basis of the morphological criteria of Trask (1971). In this system, class 5 craters are the freshest and have crisp rims, well-preserved ejecta, and visible rays. Class 4 craters have few superimposed craters and fresh ejecta and rims, but no visible rays. Class 3 craters have degraded rims and terraces and may have been infilled by smooth plains.

Class 2 craters lack visible ejecta, may have some volcanic infilling, and have numerous superimposed craters. Finally, class 1 craters may have only a partially preserved rim (for further details see McCauley et al., 1981; Spudis and Prosser, 1984; Spudis and Guest, 1988; Barnouin et al., 2012). The focus of this study is on craters of classes 3–5, though several class-2 craters are also included (see Section 4.4).

3.2.2. Target terrain

Craters were identified as hosted by either smooth plains or cratered terrain. The smooth plains are primarily volcanic in origin, sparsely cratered, and level to gently sloping (Trask and Guest, 1975; Denevi et al. 2013). The cratered terrain is the term adopted here for older terrain that surrounds smooth plains deposits and includes the intercrater plains, heavily cratered terrain, and basin ejecta units defined on the basis of Mariner 10 images (Trask and Guest, 1975). We used the map of smooth plains derived from MDIS images by Denevi et al. (2013) as a guide to determine the surrounding terrain type for each crater measured.

3.2.3. Crater type

The craters in this study were identified as simple, complex with a central peak, or complex with a central ring. Simple craters were identified on the basis of a bowl-shaped interior, possibly with a flat floor, but without a central uplift. Complex craters were identified on the basis of a central uplift structure (either a central peak or central ring). Central rings were differentiated from central peaks by the distinctive ring geometry and continuation of the flat floor inside the ring. For most craters, this identification was made from the MDIS base map and

individual monochrome images, but for smaller (D = 3–20 km) high-latitude craters (with the interior shadowed) this identification was made from the MLA transects.

3.2.4. Secondary craters

Secondary craters were also measured in this study. These craters were distinguishable from the primary craters listed in Table A1 in Appendix 1, but measurements were made with the same methods as those outlined in section 3.1. Secondary craters form by the impact of both clusters of blocks and individual blocks ejected during the formation of a (larger) primary crater. These projectiles are more likely to have lower velocities and impact at more oblique angles than for primary impacts (e.g., Schultz and Gault, 1985). Secondary craters were identified as small craters in linear arrays or clusters, usually, but not always, in the vicinity of larger impact craters. These secondary craters lack crisp rims, are often elliptical, and commonly are found in crater chains. Because of higher impact velocities on Mercury than on other terrestrial planets, secondary craters can be larger (at diameters less than 10 km secondary craters are more abundant than primary craters, Strom et al., 2008). The morphology of large secondary craters may lack some of the standard diagnostics of secondary craters elsewhere (because of their size and lack of association with either a cluster of craters or a crater ray), and some of these secondary craters may therefore have been included in the primary population examined in this study. Each crater was inspected for indicators of secondary crater morphology, and we are confident that the majority of craters reported here as primaries are actual primary craters. However, some of the small-to-medium-sized craters (D < ~20 km) in our study population could nonetheless be secondary craters that are far from their primary and lack classical secondary crater morphological features.

3.3. Transition diameter

The diameter D_t at which craters transition, with increasing diameter, from simple to complex morphology was calculated from both the quantitative and qualitative indicators of the onset of complex crater geometry, following the method outlined by Pike (1980, 1988). In this method the transition diameter is calculated from the intersection of power laws fit separately to depth/diameter (*d/D*) versus rim height/diameter (*h/D*) data for simple and complex craters, as well as the diameter of the smallest complex crater and the diameter of the largest simple crater. It also makes use of such morphologic attributes as the median diameter of the onset of flat floors (visible in MLA transects), wall slumps (wall failure that appears to be contemporaneous with the final stages of crater formation), and terraces (distinct blocks on the walls of the crater). All of these attributes were used to calculate a geometric mean diameter that reflects the morphologic transition from simple to complex crater forms on Mercury.

4. Results

We present the results obtained from measuring the geometry of 331 primary impact craters on Mercury (less than the number of craters identified in Mercury's northern hemisphere by Fassett et al. (2011) as a result of our selection criteria outlined in section 3) from data obtained during the orbital phase of the MESSENGER mission (see Table A1 in Appendix 1 and Fig. 2 for locations of the craters). First, we describe the power laws used to investigate relations between depth, rim height, or wall width and diameter. Data on secondary crater depth and rim height are compared with primary crater morphometry. Finally, a new D_t value for Mercury is calculated.

Few of the craters measured had morphologies indicative of low-angle impacts, such as asymmetric ejecta deposits, rays, or crater wall width (e.g., Gault and Wedekind, 1978; Schultz, 1992). In the analysis process we excluded craters with these morphologies (to better understand the other factors that may be contributing to crater morphometry variations), and thus, the results below minimize impact-angle effects (the craters in Table A1 in Appendix 1 do not include craters identified as resulting from low-angle impacts).

4.1. Power laws fit to the measurements for simple and complex craters

Power laws were fit to measurements of d versus D and h versus D for the population of simple craters and independently for the population of complex craters, and a power law was fit to measurements of w versus D for complex craters. Results were analyzed for both the entire crater population and for only the freshest craters (classes 4 and 5). We looked specifically at class-4 and class-5 craters because their shapes have not been substantially modified by post-impact degradation. For the fits to data from the simple crater population, only craters 5–10 km in diameter were used. The lower bound of 5 km in diameter was chosen because of the difficulties mentioned above with measuring the depths of smaller craters, e.g., as a result of MLA not sampling the deepest portion of the crater floor. The upper bound of 10 km was chosen to avoid craters that may be transitional to complex morphologies (this diameter value was chosen after evaluating the break in slope in Fig. 3). Likewise, a 15-km-diameter lower bound was chosen for the complex crater population to avoid including craters with simple-crater morphologic characteristics.

4.2. Depth versus diameter

As with other terrestrial planets, the depth (*d*) of impact craters on Mercury scales with increasing diameter (*D*) (Fig. 3). A noticeable break in slope in the relation between *d* and *D* occurs at a diameter of approximately 8–11 km; that break marks the approximate transition between simple and complex craters. The relation between *d* and *D* is broadly similar to that reported by Pike (1988) from images acquired during the Mariner 10 flybys, but several important differences can be observed. Large complex craters in this study are shallower than the Pike (1988) measurements, consistent with results reported by Barnouin et al. (2012) from the MESSENGER flybys. An example of this difference is the complex crater Brahms (centered at 58.30ºN, 182.72ºE, D = 97.3 ± 1.6 km). This crater was reported to be >3.15 km deep by Pike (1988), but MLA profiles show the depth to be 2.8 ± 0.1 km. The difference is likely due to inaccuracies in the original shadow-based measurements of depth, either because of the difficulty in measuring shadows over broad crater walls with extensive slump blocks or poor viewing geometry.

Several complex craters are outliers to the general population. Close inspection of these craters with MDIS images shows that their interiors have been modified subsequent to impact (e.g., by superposed younger craters or the formation of pits, Fig. 4). A few large simple craters (6–10 km in diameter) are deeper than the range Pike (1988) reported, but the majority of simple craters (3–10 km in diameter) are consistent with the results of his study. Further inspection of the anomalously deep simple craters using MDIS images did not reveal any clear reason (such as those associated with larger craters) for the differences in depth. Therefore, these craters are interpreted to have larger depths than typical as a direct result of their formation.

The power laws fit to *d* versus *D* for a variety of subsets of the impact crater population are reported in Table 1. The fits are compared with results from MESSENGER flyby altimetry

and imaging data (Barnouin et al., 2012), orbital MLA data acquired for craters at high northern latitudes (Talpe et al., 2012), and Mariner 10 flyby images (Pike, 1988). The power law fit to measurements for the fresh (classes 4 and 5) simple crater population has a shallower slope than that for the entire sampled population for this crater morphology. For complex craters, the slope of the power law for the fresh crater population and the entire population are both less than the slope reported by Pike (1988). This difference is the result of the smaller depths of large complex craters in this study, as mentioned above.

4.3. Measurements of rim height, wall width, and central uplift height

Our database indicates that crater rim height increases with diameter (Fig. 5), and a clear break in slope is observed between simple and complex craters (at ~11 km diameter). The power laws fit to the data for h versus D for complex craters have shallower slopes than the equivalent laws for simple craters. The power laws for both the fresh (classes 4 and 5) simple craters and the entire sampled population of simple craters are similar to results from previous studies (Table 2).

The wall width (w) of the complex craters was measured in this study to explore the role of wall collapse, an important aspect of the transition from transient cavity to final crater morphometry. Larger wall widths may be diagnostic of substantial crater collapse. On Mercury, the relation between w and D shows little variation for smaller (D<50 km) complex craters (Fig. 6). For larger complex craters (D>60 km), in contrast, an increased spread in w is observed for a given D. The power laws fit to the data (Table 3) are similar for the fresh and entire complex crater populations.

Past studies of central uplift height (*r*) on Mercury (e.g., Pike, 1988) have documented an increase in *r* with increasing *D*, an observation that is confirmed here (Fig. 7). The relation between *r* and *D*, though, shows greater scatter than other crater morphometric relations. Central uplift height can vary by up to an order of magnitude for similarly sized small (*D* = 15–30 km) complex craters. For large complex craters, variations in central uplift height are smaller in relative magnitude but can still exceed 1 km. Some of the variation can be attributed to MLA range measurements not always sampling the very highest portion of the central uplift. We did not calculate power laws because of the large scatter within the data set for *r* versus *D*.

4.4. Crater morphological class

Crater degradation influences crater morphometry. Fresh impact craters are usually deeper than older and more degraded craters (Fig. 8a), as previously reported for Mercury (e.g., Pike, 1988; Barnouin et al., 2012), although there are some deviations from this trend. For example, within the freshest crater population (classes 4 and 5), some variations in *d* are observed across all diameters (no systematic variations in *d* are observed between class-4 and class-5 craters). These differences in depth (see example in section 4.2) can be up to 30–50% of the total depth of the crater and are not always correlated with terrain type. These differences are much larger than the 200–300 m variation in depth found in complex craters on the Moon (Kalynn et al., 2013).

Crater degradation on Mercury also affects rim height and central uplift height. Relations between *h* and *D* and between *r* and *D* (Fig. 8b,c) depend on degradation, with the freshest craters (class 5) having the largest *h* and *r* values for a given *D*. Within the other fresh (class 4) and moderately degraded (class 3) classes of craters, the spreads in the relations for *h* versus *D*

and *r* versus *D* are comparable. No clear dependence of *w* versus *D* on degradation is observed (Fig. 8d).

4.5. Target geology

Differing target properties among geologic units is known to influence crater morphometry. On the Moon, complex craters in the maria are generally shallower than craters in the highlands (Pike, 1974; Kalynn et al., 2013). On Mars, distinct geological units show distinct *d/D* values for simple craters (Boyce et al., 2006; Stewart and Valiant, 2006; Robbins and Hynek, 2012a,b). On Mercury, individual crater depths may be slightly deeper within the cratered terrain than in the smooth plains (Fig. 9a), but such a difference cannot be established with significance for the entire population. More craters were measured in the smooth plains than the cratered terrain due to issues in properly capturing the rim heights of craters (from difficulties in fitting a plane to the surrounding terrain) in the cratered terrain. Since no statistically significant difference is found between crater populations in the different terrains, no bias was introduced into our overall measurements of crater morphometry. The relations for *h* versus *D*, *r* versus *D*, and *w* versus *D* show no clear dependence on target geology (Fig. 9b–d).

4.6. Secondary craters

The morphologies of secondary craters on Mercury are similar to those on other bodies. Secondary craters (see Table A2 in Appendix 1) are usually shallower than simple primary craters (Fig. 10a). The smaller *d* is expected as a result of the lower impact velocities (<4.3 km/s, Mercury's escape velocity), the likely clustered nature of many secondary impactors, and often oblique impact angles (the result of blocks ejected on ballistic trajectories from the primary

crater) of the impactors. The spread in *d* versus *D*, though, does overlap with that for primary craters. The relation for *h* versus *D* for secondary craters (Fig. 10b) shows no clear difference from that for primary craters.

4.7. Transition diameter

The high-resolution topography from MESSENGER permits a new estimate of D_t for Mercury to be calculated and compared with the D_t value for Mars. On Mercury, the intercept of the power laws for relations between *d* and *D* for fresh simple and complex craters indicates a D_t value of 10.2 km, larger than the value reported by Talpe et al. (2012). The other morphologic indicators that differ between simple and complex morphologies show transitions at different onset diameters. The median diameter of the onset of flat floors occurs at D = 9.6 km, that for wall slumps at D = 10.3 km, that for terraces at D = 14.4 km, and that from the intersection of the power laws fit to relations between *h* and *D* for simple and complex craters at D = 13.0 km. When all morphologic indicators are considered (Fig. 11a–c, Table 4; see section 3.3), the best overall estimate of D_t is 11.7 ± 1.2 km, a result consistent with the Mariner 10 (Pike, 1988) and MESSENGER (Barnouin et al., 2012) flyby results.

5. Discussion

The morphometric relations of impact craters on Mercury measured from MESSENGER data are similar to those reported previously, with crater depth, rim height, wall width, and central uplift height increasing with increasing diameter (Pike, 1988; Barnouin et al., 2012; Talpe et al., 2012). Variations in morphometry are consistent with a transition from simple to complex craters at a diameter of ~12 km. The spread in wall width for larger-diameter craters could be

evidence of the beginning of the transition from complex crater to basin morphologies. Baker et al. (2011) identified the onset diameter for peak-ring basins at $126\,^{+33}_{-26}$ km, larger than the diameter (~60 km) at which wall width begins to vary, but their study included peak-ring basins as small as 83 km in diameter (within the range of diameters of craters in this study that display a large spread in *w* at a given *D*). Although these broad trends in crater morphology hold in general, small deviations throughout the population provide insight into the impact cratering process, and are of interest when comparing crater geometry on Mercury to that on Mars (since both bodies have similar surface gravitational acceleration).

5.1. Target properties

We compared the morphometry of craters in different geologic units on Mercury for insight into their relative physical properties (e.g., strength or porosity). Fresh complex craters in the cratered terrain may be slightly deeper than similar-sized craters in the smooth plains, but any differences in depth are not statistically significant. The lack of a significant difference in the depth of craters between geologic terrains on Mercury could be due to a smaller age difference between the smooth plains and cratered terrains relative to the larger age difference between the maria and highlands on the Moon. The possible volcanic origin of both the intercrater plains (e.g., Trask and Guest, 1975; Whitten et al., 2014) and smooth plains (e.g., Trask and Guest, 1975; Spudis and Guest, 1988; Denevi et al., 2013) may also contribute to reducing the difference in crater depth between the two units (when compared with the lunar maria and highlands, which have different origins). Other factors that may contribute to the difference in observable terrain effects between craters on Mercury and on the Moon include the the higher surface gravitational acceleration of Mercury (which requires stronger rocks to resist

gravitational collapse) and the wider range in impact velocities at Mercury, the effect of which may overwhelm other factors (see section 5.3). This mix of possible contributing factors implies that the significant difference in depth between individual craters such as the class-5 craters Fonteyn and Cunningham (Fig. 12) is probably not a consequence of the different terrains in which they formed (since no similar differences are seen in neighboring fresh craters), but is due to some other difference in their formation process. The lack of difference in *d/D* between terrains on Mercury also differs from results for simple craters on Mars, where differences in *d/D* among different geologic units have been observed (Boyce et al., 2006; Robbins and Hynek, 2012b, 2013). However, the Mercury results are similar to those on Mars for complex craters, where statistical analyses show no variations in *d/D* with differing terrain (Boyce and Garbeil, 2007; Robbins and Hynek, 2012a,b, 2013).

5.2. Crater morphological class

Since fresh craters are used to calculate the D_t value, sampling was focused on crater classes 3 and higher. For the morphological classes examined in this study (including the few class-2 craters measured), the freshest craters (class 5) tend to be the deepest, but variations in depth are seen even within the freshest morphological class. Likewise, rim height is reduced with degradation state, whereas wall width remains unchanged. The decrease in crater depth and rim height can be attributed to the action of later small impacts that erode the rims and infill the crater with ejecta, a finding consistent with previously reported observations (Wood et al., 1977; Pike, 1980, 1988; Barnouin et al., 2012).

5.3. Impact velocity

Within the fresh (classes 4 and 5) to moderately fresh (class 3) crater populations, most craters of a given size show little to no variation in depth. There nonetheless are a few craters where significant differences in depth are seen that do not correlate with geologic unit or state of crater degradation. The differences in depth of these craters are larger than those found on Mars (e.g., Robbins and Hynek, 2013) and the Moon (Kalynn et al., 2013) in fresh craters within the same geologic unit. An example of this variability (Fig. 13) is provided by craters Atget (25.6ºN, 166.42ºE; D = 102 ± 1.1 km; d = 3.2 ± 0.5 km; class 4) and Hokusai (57.69ºN, 16.87ºE; D = 97.3 ± 1.1 km; d = 2.3 ± 0.2 km; class 5). The two craters differ in depth by 0.9 km, well in excess of their associated measurement errors. Both craters are also within the smooth plains as mapped by Denevi et al. (2013), so neither degradation nor target character is likely to have caused the large depth difference.

Dynamical models indicate that a large range in impact velocity (20–65 km/s) is expected at Mercury, a range substantially greater than for other planets in the inner solar system (Le Feuvre and Wieczorek, 2008; Marchi et al., 2012). High-velocity impacts on Mercury have also been previously cited as an explanation for the higher rim crests of craters on Mercury than on the Moon (Cintala, 1979).

Laboratory cratering experiments have documented an increase in transient crater depth with decreasing projectile velocity, as a result of the increased penetration of lower-velocity projectiles (Schultz, 1988; Barnouin et al., 2011). During a low-velocity impact, the time of contact (coupling) between the target and projectile is longer than during a high-velocity event. Because the shock wave travels more slowly through the projectile (because of the lower initial velocity of the projectile), the projectile survives longer. This additional coupling time permits the projectile to penetrate deeper into the target. In laboratory experiments, this effect yields a

deep transient crater with steep walls (Barnouin-Jha et al., 2007; Barnouin et al., 2011). The steep walls collapse more fully than walls produced by faster projectiles, resulting in a shallower final crater (Schultz, 1988; Barnouin et al., 2011).

Simple hydrodynamic analyses (e.g., Gault and Heitowit, 1963; Cheng et al., 1999) also indicate that projectile speed differences could substantially influence the normalized penetration depth of an impactor relative to crater diameter. A numerical study of the lower range of impact velocities for simple craters on Pluto shows an increase in the *d/D* ratio of craters with increasing impact velocity and then a gradual decrease (at an inflection point) to a steady leveling off of *d/D* with further increases in velocity above ~2 km/s (Bray and Schenk, 2014). This study was performed for icy targets with different surface strengths and properties than expected on Mercury. The Bray and Schenk results align with experimental evidence for the low range of impact velocities, but differs for velocities 3–6 km/s, for which laboratory results show *d/D* continuing to increase with velocity (Barnouin et al., 2011). Bray and Schenk (2014) noted that the details of the *d/D* variation with velocity changes with different model parameters. A study using a different numerical algorithm suggests that the inflection in *d*/*D* versus velocity could occur at a velocity of 5 km/s (Jutzi and Michel, 2014), which might explain why no inflection point is observed in the laboratory. The inflection point could also explain why the majority of craters on Mercury show little variation in *d/D* even with the high expected range in velocity. Nevertheless, craters Hokusai and Atget show a large difference in depth, and impact velocity cannot be ruled out as a factor.

5.4. Comparing transition diameter and crater depth on Mercury and Mars

Mercury and Mars provide a means to explore the roles of projectile and target properties on crater morphometry in a natural experiment, in which the surface gravitational acceleration is held approximately constant. The transition diameter D_t for Mercury is 11.7 ± 1.2, whereas the global D_t value for Mars is 5.6 ± 1.2 (Robbins and Hynek, 2012b), confirming the difference in D_t found in previous studies (Pike, 1980, 1988).

No statistical difference exists between *d/D* values for Mercury relative to those for Mars at a given *D* (Fig. 14). The similarity in *d/D* on Mars and Mercury is in contrast to reports from prior studies, mainly due to recent studies of the *d/D* ratio on Mars. For Mars, Robbins and Hynek (2012b) distinguish between deepest and fresh craters when generating their *d/D* fits. The deepest-crater method most likely captures the original depths of Martian craters (Boyce and Garbeil, 2007; Robbins and Hynek, 2012b) given the high the erosional rates on Mars. On Mercury, the distinction between deepest and fresh craters is not relevant, for two reasons: (1) the erosion rate on Mercury is lower; and (2) some of the freshest craters on the planet (e.g., Hokusai) are among the shallowest at their diameter. The comparison in Fig. 14 is for deepest crater results for Mars. What then drives the difference in D_t, but not crater depth, between these two bodies? Previous studies (e.g., Pike, 1980, 1988) cited surface properties as the source, including different volatile contents and geologic histories. Past authors proposed that weaker rocks on Mars collapse at a smaller diameter to form complex craters, whereas on Mercury the stronger rocks resist collapse until a larger diameter is reached. But such a proposal is not consistent with the similar *d/D* values for the two bodies for simple craters. Recall that for Mars, *d/D* for simple craters and D_t change with terrain, and these changes are thought to be a consequence of target strength. This result potentially negates the importance of strength in

controlling the difference in D_t between Mercury and Mars, given that the relations between *d/D* and *D* for simple craters on the two bodies are not statistically different.

Can different impact velocities account for the difference in D_t but maintain the similarity in *d/D* versus *D* for simple craters on Mars and Mercury? In laboratory experiments, higher-velocity impacts can produce deeper final craters (Barnouin et al., 2011), at least for velocities less than a specific impact velocity at which an inflection point occurs in the relation with velocity (Jutzi and Michel, 2014; Bray and Schenk, 2014). On Mars, where the average impact velocity is lower, this effect would produce deeper transient craters than the shallower transient craters on Mercury. The Martian transient craters could collapse at a smaller diameter and generate complex craters with a smaller transition diameter than on Mercury. If the transient cavities on Mars were deeper, shallower final craters would most likely result (because of the substantial collapse of the transient crater walls), but this effect is not observed. The combination of different D_t values for Mercury and Mars and a similar *d/D* relation with *D* for simple craters is not well explained by our current understanding of the effects of either target properties or variations in impact velocity. Further research on how both factors influence final crater morphology is warranted.

5.5. Transition diameter

The transition from simple to complex morphology begins, with increasing crater diameter, with a change in the crater depth at a given crater diameter. This effect is followed, with crater diameter increasing further, by the gradual transition to a flat floor, wall slumping, the appearance of a central peak, terracing, and finally a change in the rim height. This pattern

(Fig. 15) was documented at Mercury by Pike (1988) and is seen as well on the Moon (Shoemaker, 1962).

This sequence in the development of the morphological characteristics of complex craters with increasing diameter can guide understanding of the processes that drive the formation of complex craters. The early onset of the change in depth and the appearance of flat floors is supported by experimental (e.g., Barnouin-Jha et al., 2007) and numerical (e.g., O'Keefe and Ahrens, 1993) evidence that, as craters grow, they first reach a maximum depth but continue to grow laterally. Some inevitable wall collapse in the last stage of the cratering process widens and shoals the crater floor further, with impact melt pooling at the bottom of the crater. The collapse first leads to terracing and eventually, with sufficient terracing and collapse, the reduction of rim-height. Isostatic rebound will also contribute to the flattening of a crater and the elevation of the central uplift (Pike, 1988).

6. Conclusions

MESSENGER's orbital mission phase has provided the needed coverage by MLA and MDIS to quantify the morphometry of Mercury's impact craters and to provide a new and more comprehensive determination of the transition diameter from simple to complex craters. The observations have been compared with previous studies of craters on Mercury, and with studies of crater morphometry on the Moon and Mars. The main results of the study indicate:

1. Crater depth, rim height, wall width, and central uplift height all increase with increasing crater diameter. The depths of large complex craters are shallower than those inferred from Mariner 10 images (Pike, 1988) but are consistent with measurements made from MESSENGER flyby data (Barnouin et al., 2012).

2. An updated value of the diameter (D_t) of 11.7 ± 1.2 km marking the transition with increasing diameter from simple to complex craters on Mercury was calculated using the methodology described by Pike (1980, 1988). This value differs from D_t for Mars (5.6 ± 2.3 km; Robbins and Hynek, 2012b), even though both bodies have nearly identical surface gravitational acceleration. No statistical difference in the relation between *d/D* and *D* for simple craters is found between Mercury and Mars.
3. Near-field secondary craters on Mercury are typically shallower than primary craters, although rim heights appear similar.
4. Within the fresh crater population (for craters in the same geologic province), variations in crater depth may be observed. This variability may be evidence for velocity-driven variations in crater depth on Mercury, the result of Mercury's large range in expected projectile velocities (e.g., Le Feuvre and Wieczorek, 2008).
5. Depths of craters within the cratered terrain and of craters in the smooth plains are not statistically distinguishable.
6. The transition from simple to complex crater morphology does not appear at the same crater diameter for all of the morphological attributes. For the craters measured in this study, crater depth and floor shape are modified at a smaller diameter than crater rim and walls and at a smaller diameter than that at which central peaks first appear.

7. Acknowledgements

We thank Robert Herrick and an anonymous reviewer for thoughtful reviews that greatly improved this paper. We thank Clark Chapman, Steven Hauck, Lillian Ostrach, Gregory Neumann, and Sean Solomon for helpful comments on earlier drafts of this paper. We gratefully

acknowledge funding from the MESSENGER project, which is supported by the NASA Discovery Program under contract NASW-00002 to the Carnegie Institution of Washington, contract NAS5-97271 to The Johns Hopkins University Applied Physics Laboratory, and the MESSENGER Participating Scientist Program. CLJ acknowledges support from the Natural Sciences and Engineering Research Council of Canada. HCMS also acknowledges support from a Johns Hopkins Applied Physics Laboratory Graduate Research Fellowship.

8. References

Baker, D.M.H, et al., 2011. The transition from complex crater to peak-ring basin on Mercury: New observations from MESSENGER flyby data and constraints on basin formation models. Planet. Space Sci. 59, 1932–1948.

Barnouin, O.S., et al., 2011. Experimental results investigating the impact velocity effects on crater growth and the transient crater diameter-to-depth ratio. Lunar Planet Sci. 42. Abstract 2258.

Barnouin, O.S., et al., 2012. The morphology of craters on Mercury: Results from MESSENGER flybys. Icarus 219, 414–427.

Barnouin-Jha, O.S., Baloga, S., Glaze, L., 2005. Comparing landslides to fluidized crater ejecta on Mars. J. Geophys. Res. 110, E04010. http://dx.doi.org/10.1029/2003JE002214.

Barnouin-Jha, O.S., et al., 2007. Non-intrusive measurements of crater growth. Icarus 188, 506–521.

Bray, V.J., Schenk, P.M., 2014. Pristine impact crater morphology on Pluto – Expectations for New Horizons. Icarus 246, 156–164.

Boyce, J.M., Garbeil, H., 2007. Geometric relationships of pristine Martian complex impact craters, and their implications to Mars geologic history. Geophys. Res. Lett. 34, L16201. http://dx.doi.org/10.1029/2007GL029731.

Cintala, M.J., 1979. Mercurian crater rim heights and some interplanetary comparisons. Proc. Lunar Planet. Sci. Conf. 10, 2635–2650.

Cintala, M.J., Head, J.W., Mutch, T.A., 1977a. Characteristics of fresh martian craters as a function of diameter: Comparison with the Moon and Mercury – Discussion. Geophys. Res. Lett. 4, 245–246.

Cintala, M.J., Wood, C.A., Head, J.W., 1977b. The effects of target characteristics on fresh crater morphology: Preliminary results for the Moon and Mercury. Proc. Lunar Sci. Conf. 8, 3409–3425.

Cheng, A.F., Barnouin-Jha, O.S., 1999. Giant craters on Mathilde. Icarus 140, 34–48.

Denevi, B.W., et al., 2013. The distribution and origin of smooth plains on Mercury. J. Geophys. Res. Planets 118, 891–907.

Fassett, C.I., et al., 2011. The global population of large craters on Mercury and comparison with the Moon. Geophys. Res. Lett. 38, L10202. http://dx.doi.org/10.1029/2011GL047294.

Fulmer, C.V., Roberts, W.A., 1963. Rock induration and crater shape. Icarus 2, 452–465.

Garvin, J.B., Frawley, J.J., 1998. Geometric properties of martian impact craters: Preliminary results from the Mars Orbiter Laser Altimeter. Geophys. Res. Lett. 25, 4405–4408.

Gault, D.E., Heitowit, E.D., 1963. The partition of energy for hypervelocity impact craters formed in rock. Proc. Sixth Hypervelocity Impact Symposium, vol. 2. Firestone Tire and Rubber Co., Akron, Ohio, pp. 419–456.

Gault, D.E., Wedekind, J.A., 1978. Experimental studies of oblique impact. Proc. Lunar Planet. Sci. Conf. 9, 3843–3875.

Gault, D.E., Quaide, W.L., Oberbeck, V.R., 1968. Impact cratering mechanics and structure. In: French, B.M., Short, N.M. (Eds.), Shock Metamorphism of Natural Materials. Mono Book Corp., Baltimore, Md., pp. 87–99.

Glaze, L.S., Baloga, S.M., Stofan, E.R., 2003. A methodology for constraining lava flow rheologies with MOLA. Icarus 165, 26–33.

Hartmann, W.K., 1981. Discovery of multi-ring basins: Gestalt perception in planetary science. In: Merrill, R.B., Schultz, P.H. (Eds.), Multi-ring Basins: Formation and Evolution.

Pergamon Press, New York, pp. 79–90.

Hermalyn, B., Schultz, P.H., 2011. Time-resolved studies of hypervelocity vertical impacts into porous particulate targets: Effects of projectile density on early-time coupling and crater growth. Icarus 216, 269–279.

Herrick, R.R., Forsberg-Taylor, N.K., 2003. The shape and appearance of craters formed by oblique impact on the Moon and Venus. Meteorit. Planet. Sci. 38, 1551–1578.

Hessen, K. K. et al., 2007. Low-velocity oblique impact experiments in a vacuum. Lunar Planet. Sci. 38. Abstract 2141.

Holsapple, K.A., 1993. The scaling of impact processes in planetary sciences. Annu. Rev. Earth Planet. Sci. 21, 333–373.

Horedt, G.P., Neukum, G., 1984. Planetocentric versus heliocentric impacts in the jovian and saturnian satellite system. J. Geophys. Res. 89, 10405–10410.

Housen, K.R., Holsapple, K.A., 2003. Impact cratering on porous asteroids. Icarus 163, 102–119.

Jutzi, M. Michel, P., 2014. Hypervelocity impacts on asteroids and momentum transfer I. Numerical simulations using porous targets. Icarus, 229, 247–253.

Kalynn, J., et al., 2013. Topographic characterization of lunar complex craters. Geophys. Res. Lett. 40, 38–42.

Le Feuvre, M., Wieczorek, M.A., 2008. Nonuniform cratering of the terrestrial planets. Icarus 197, 291–306.

Marchi, S., et al., 2012. The violent collisional history of asteroid 4 Vesta. Science 336, 690–694.

McCauley, J.F., et al., 1981. Stratigraphy of the Caloris basin, Mercury. Icarus 47, 184–202.

Neukum, G., Ivanov, B.A., 1994. Crater size distributions and impact probabilities on Earth from

lunar, terrestrial-planet, and asteroid cratering data. In: Gehrels, T., Matthews, M.S., Schumann, A.M. (Eds.), Hazards due to Comets and Asteroids. University of Arizona Press, Tucson, Ariz., pp. 359–416.

O'Keefe, J.D., Ahrens, T.J., 1993. Planetary cratering mechanics. J. Geophys. Res. 98, 17011–17028.

Pike, R.J., 1974. Depth/diameter relations of fresh lunar craters: Revision from spacecraft data. Geophys. Res. Lett. 1, 291–294.

Pike, R.J., 1980. Control of crater morphology by gravity and target type: Mars, Earth, Moon. Proc. Lunar Planet. Sci. Conf. 11, 2159–2189.

Pike, R.J., 1988. Geomorphology of impact craters on Mercury. In: Vilas, F., Chapman, C.R., Matthews, M.S. (Eds.), Mercury. University of Arizona Press, Tucson, Ariz., pp. 165–273.

Robbins, S.J., Hynek, B.M., 2012a. A new global database of Mars impact craters ≥1 km: 1. Database creation, properties, and parameters. J. Geophys. Res. Planets 117, E05004. http://dx.doi.org/10.1029/2011JE003966.

Robbins, S.J., Hynek, B.M., 2012b. A new global database of Mars impact craters ≥1 km: 2. Global crater properties and regional variations of the simple-to-complex transition diameter. J. Geophys. Res. 117, E06001. http://dx.doi.org/10.1029/2011JE003967.

Robbins, S.J., Hynek, B.M., 2013. Utility of laser altimeter and stereoscopic terrain models: Application to martian craters. Planet. Space Sci. 86, 57–65.

Schultz, P.H., 1988. Cratering on Mercury: A relook. In: Vilas, F., Chapman, C.R., Matthews, M.S. (Eds.), Mercury. University of Arizona Press, Tucson, Ariz., pp. 274–335.

Schultz, P.H., 1992. Atmospheric effects on ejecta emplacement and crater formation on Venus from Magellan. J. Geophys. Res. 97, 16183–16248.

Schultz, P.H., Gault, D.E., 1985. Clustered impacts: Experiments and implications. J. Geophys. Res. 90, 3701–3732.

Schultz, P.H., Ernst, C.M., Anderson, J.L.B., 2005. Expectations for crater size and photometric evolution from the Deep Impact collision. Space Sci. Rev. 117, 207–239.

Shoemaker, E.M., 1962. Interpretation of lunar craters. In: Kopal, Z. (Ed.), Physics and Astronomy of the Moon. Academic Press, New York, pp. 283–359.

Shoemaker, E.M., 1963. Impact mechanics at Meteor Crater, Arizona. In: Middlehurst, B.M., Kuiper, G.P. (Eds.), The Moon, Meteorites and Comets. University of Chicago Press, Chicago, Ill., pp. 301–336.

Spudis, P.D., Prosser, J.G., 1984. Geological Map of the Michelangelo (H-12) quadrangle of Mercury. Map I-1659, Misc. Investigations Ser., U.S. Geological Survey, Denver, Colo.

Spudis, P.D., Guest, J.E., 1988. Stratigraphy and geologic history of Mercury. In: Vilas, F., Chapman, C.R., Matthews, M.S. (Eds.), Mercury. University of Arizona Press, Tucson, Ariz., pp. 118–164.

Stewart, S.T., Valiant, G.J., 2006. Martian subsurface properties and crater formation processes inferred from fresh impact crater geometries. Meteorit. Planet. Sci. 41, 1509–1537.

Stopar, J.D. et al., 2012. Regolith characterization using LROC NAC digital elevation models of small lunar craters. Lunar Planet. Sci. 43. Abstract 2729.

Strom, R.G., et al., 2005. The origin of planetary impactors in the inner solar system. Science 309, 1847–1850.

Strom, R.G., et al., 2008. Mercury cratering record viewed from MESSENGER's first flyby. Science 321, 79–81

Talpe, M.J., et al., 2012. Characterization of the morphometry of impact craters hosting polar

deposits in Mercury's north polar region. J. Geophys. Res. 117, E00L13. http://dx.doi.org/10.1029/2012JE004155.

Trask, N.J., 1971. Geologic comparison of mare materials in the lunar equatorial belt, including Apollo 11 and 12 landing sites. U.S. Geol. Surv. Prof. Pap. 750-D, D138–D144.

Trask, N.J., Guest, J.E., 1975. Preliminary geologic terrain map of Mercury. J. Geophys. Res. 80, 2461–2477.

Vickery, A.M., 1987. Variation in ejecta size with ejection velocity. Geophys. Res. Let. 14, 726–729.

Wieczorek, M.A., et al., 2013. The crust of the Moon as seen by GRAIL. Science 339, 671–675.

Wood, C.A., Head, J.W., Cintala, M.J., 1977. Crater degradation on Mercury and the Moon: Clues to surface evolution. Proc. Lunar Sci. Conf. 8, 3503–3520.

Zuber, M.T., et al., 2012. Topography of the northern hemisphere of Mercury from MESSENGER laser altimetry. Science 336, 217–220.

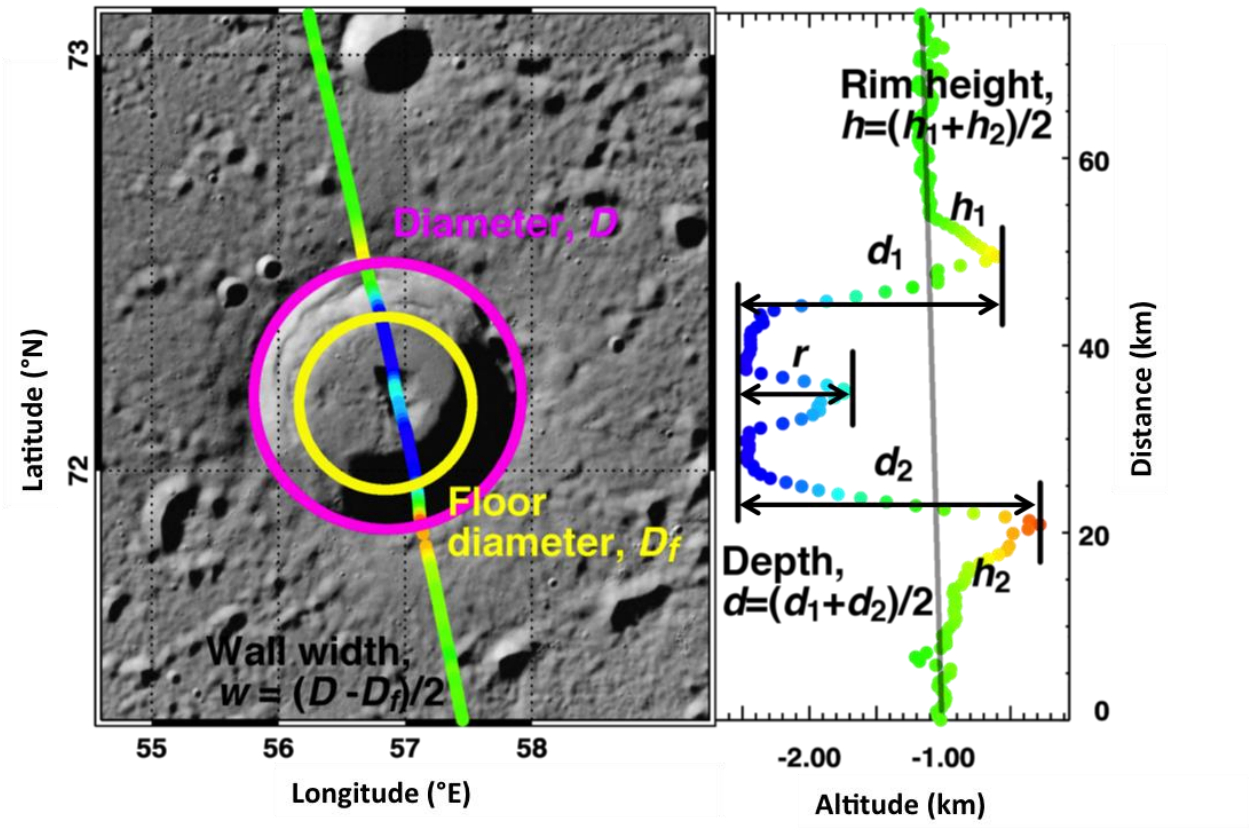

Fig. 1. Schematic illustration of the methodology for measuring crater depth (d), diameter (D), rim height (h), central peak height (r), and floor diameter (D_f) from the MLA and MDIS data. The crater shown is an unnamed, 28-km-diameter crater.

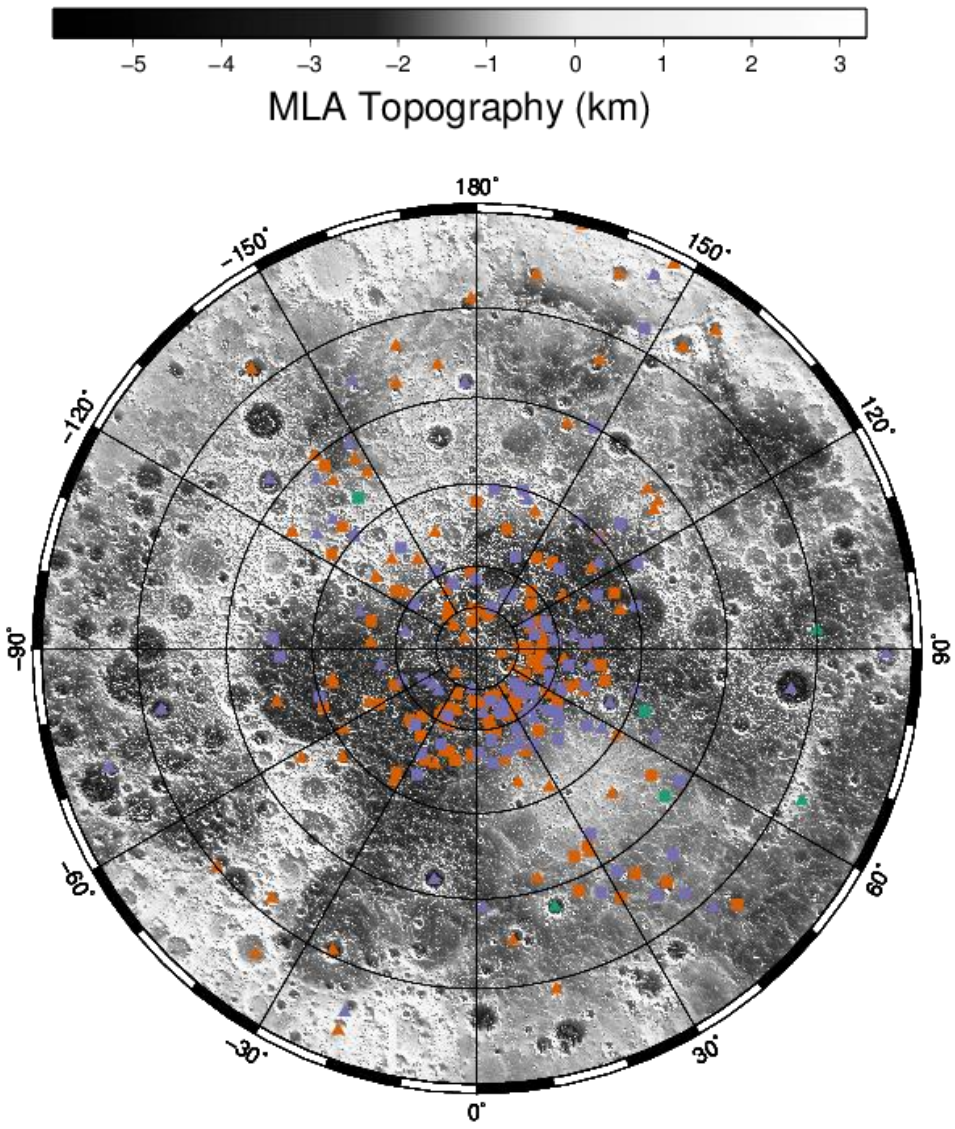

Fig. 2. Map of the locations of simple and complex craters on Mercury considered here divided by degradation class. The simple craters are represented by squares and the complex craters by triangles. Class 3 craters have orange symbols, class 4 craters have purple symbols, and class 5 craters have green symbols. The background map is the interpolated topography from MLA and ranges from 40° to 90°N. Thirty craters located south of 40°N are not shown.

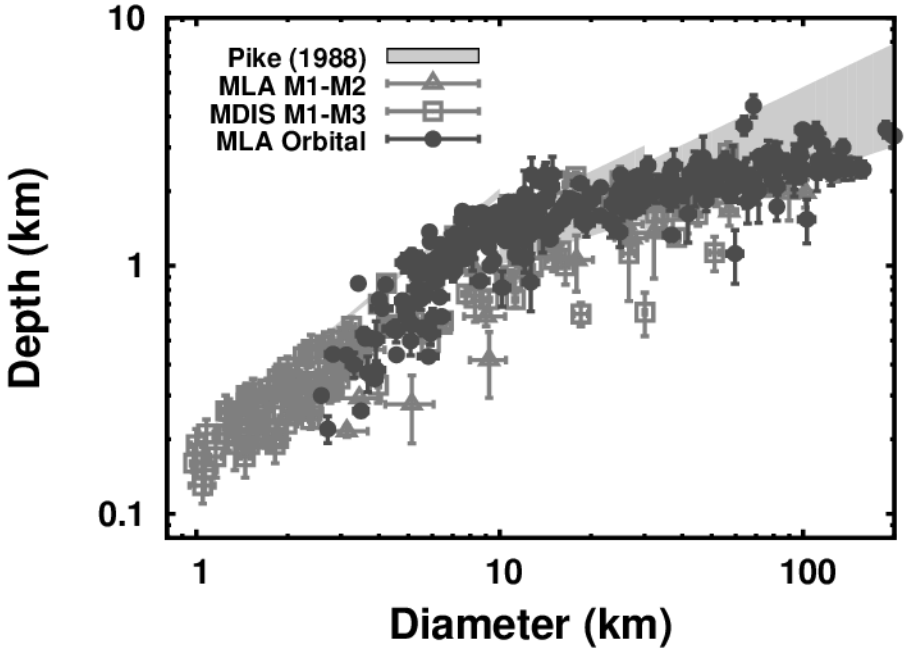

Fig. 3. Comparison of the relation between depth and diameter for the craters in this study (MLA Orbital) with results from the MESSENGER (Barnouin et al., 2012) and Mariner 10 (Pike, 1988) flybys. For the MESSENGER flybys, measurements made from MDIS images (M1–M3) and MLA (M1–M2) data are shown. The two complex craters that are outliers (both in the diameter range 60–70 km and unusually deep) compared with the main body of measurements from this study show evidence for post-impact modification (including large craters on the floor and possible volcanic vents, see Fig. 4).

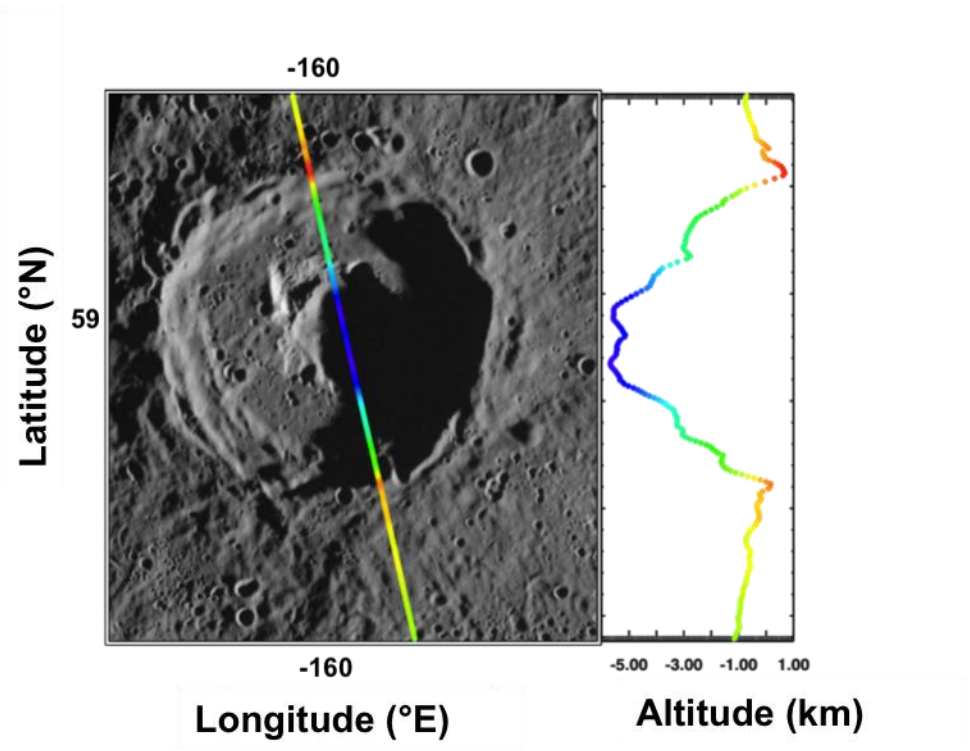

Fig. 4. The crater Navoi, 68.6 ± 3.0 km in diameter, is unusually deep (4.4 ± 0.4 km) as a result of a depression in the interior that likely postdated the formation of the crater. The depression may be volcanic in origin (e.g., a vent structure). This crater and others with obvious post-cratering modification were removed from the more detailed exploration of crater morphometry shown in Figs. 8 and 9 and from the determination of power law relations.

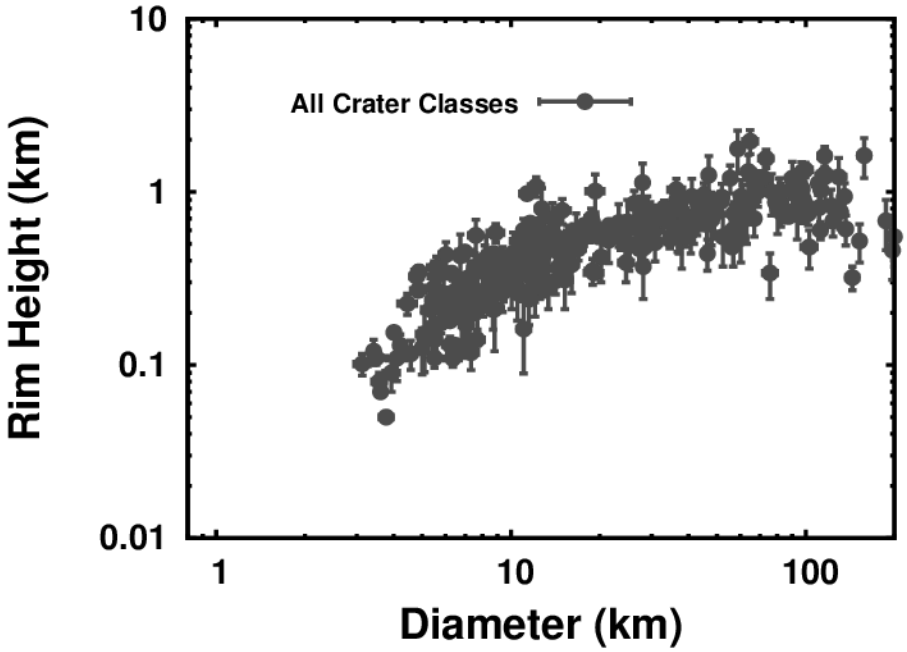

Fig. 5. Relation between the rim height (*h*) and diameter (*D)* for all craters in this study. A break in slope between the simple and complex populations can be seen at a diameter of ~11 km.

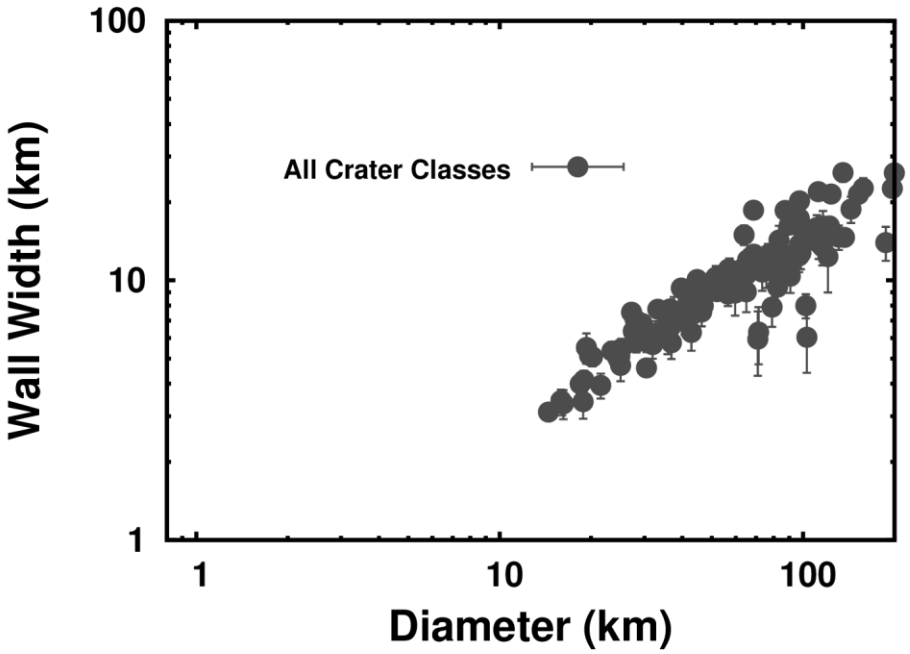

Fig. 6. Relation between wall width (*w*) and diameter (*D*) for all complex craters in this study. Note that the spread in *w* at a given *D* increases for diameters greater than ~60 km.

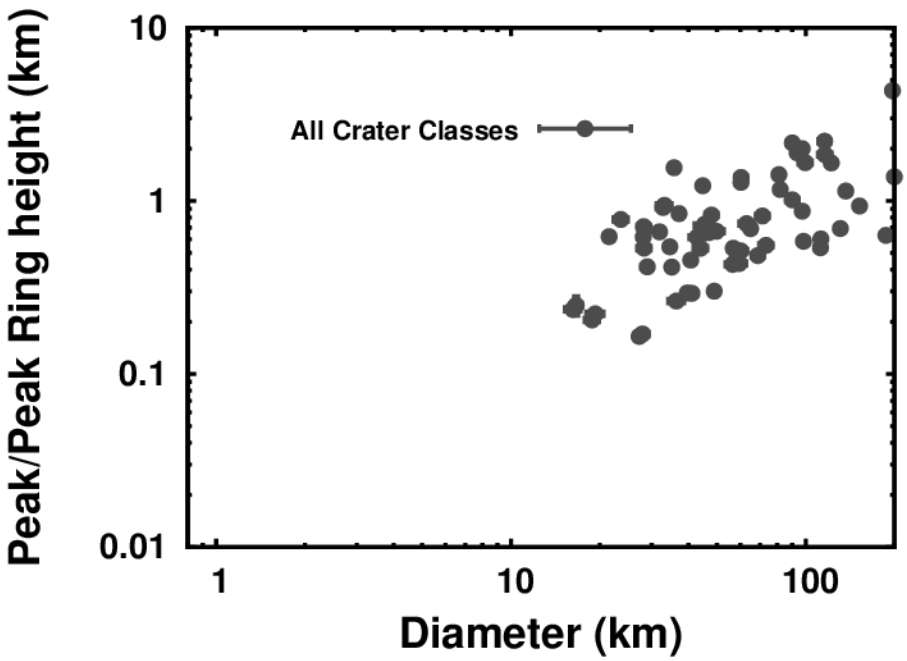

Fig. 7. Relation between central peak/ring height (*r*) and diameter (*D*) for all complex craters in this study. Note the large spread in *r* for all diameters of complex craters in this study.

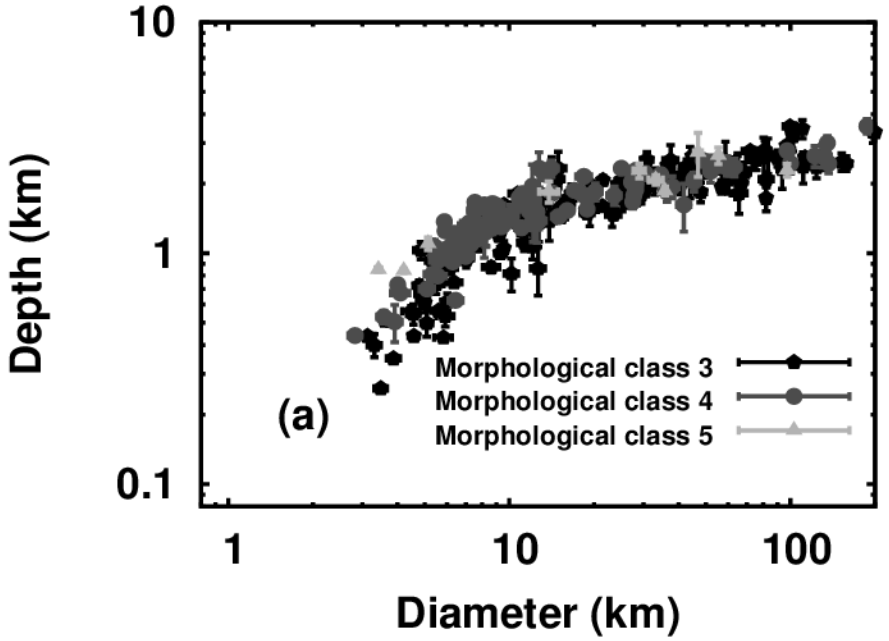
10
1
0.1
Depth (km)
1
10
100
Diameter (km)
(a)
Morphological class 3
Morphological class 4
Morphological class 5

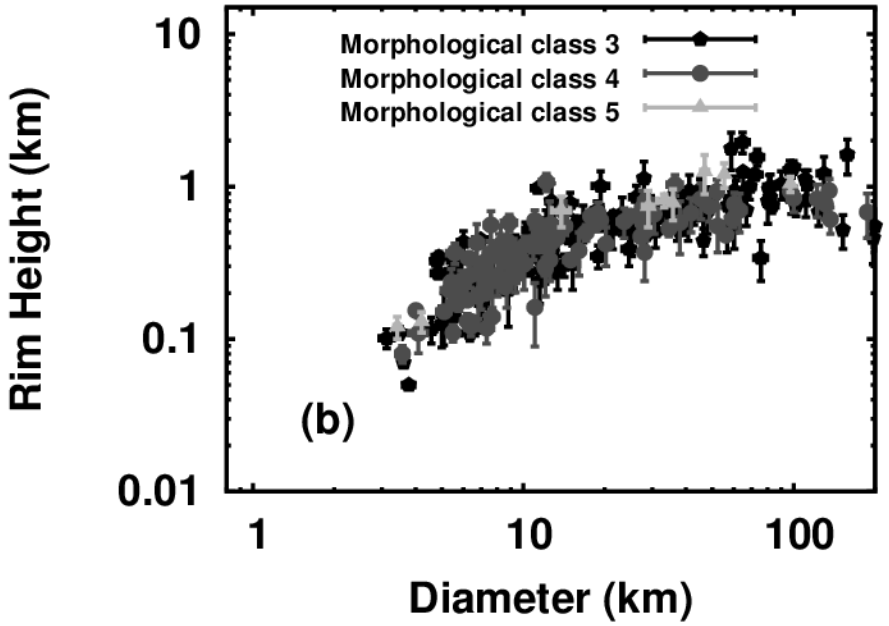
10
1
0.1
0.01
Rim Height (km)
1
10
100
Diameter (km)
(b)
Morphological class 3
Morphological class 4
Morphological class 5

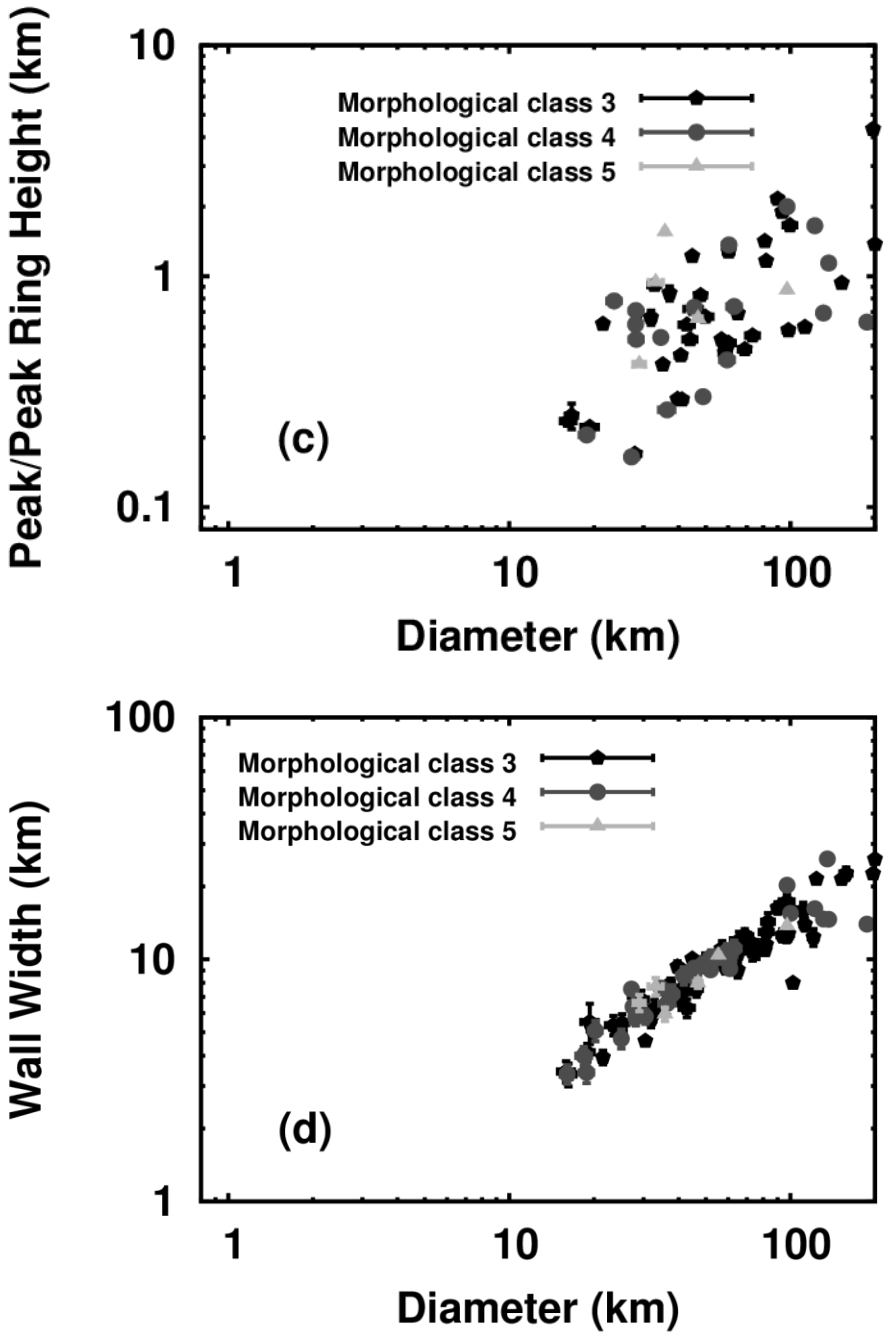

Fig. 8. Comparison of the relation between several morphological attributes and diameter for craters in morphological classes 3–5 (class-5 craters are the freshest). (a) Depth versus diameter. The deepest craters are not the necessarily the freshest. (b) Rim height versus diameter. (c) Central peak versus diameter. (d) Wall width versus diameter.

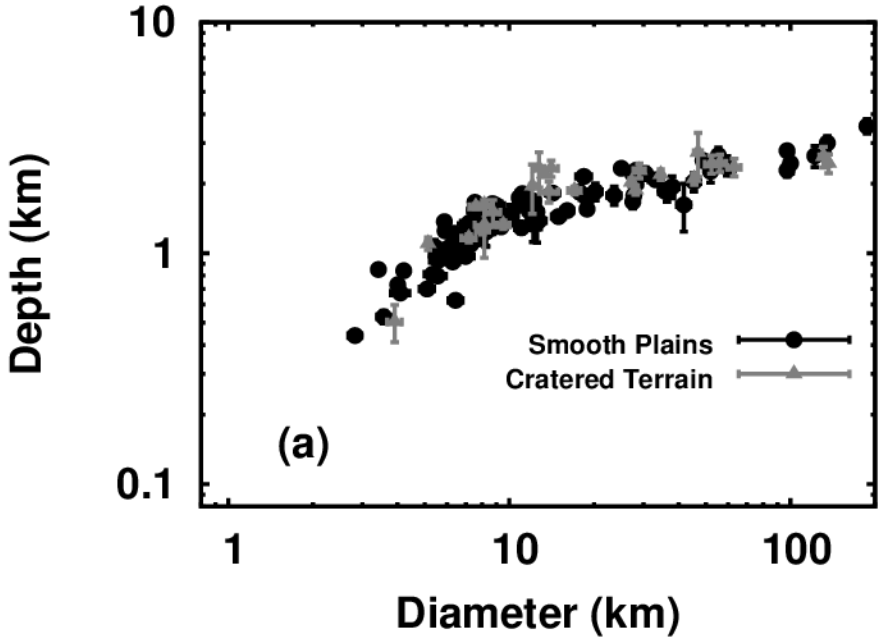
10
1
0.1
Depth (km)
Smooth Plains
Cratered Terrain
(a)
1
10
100
Diameter (km)

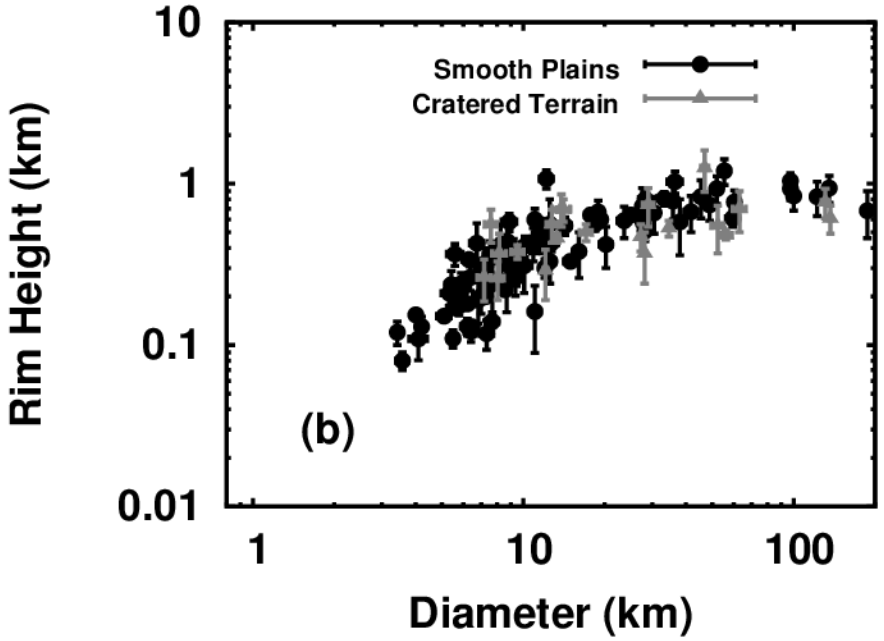
10
1
0.1
0.01
Rim Height (km)
Smooth Plains
Cratered Terrain
(b)
1
10
100
Diameter (km)

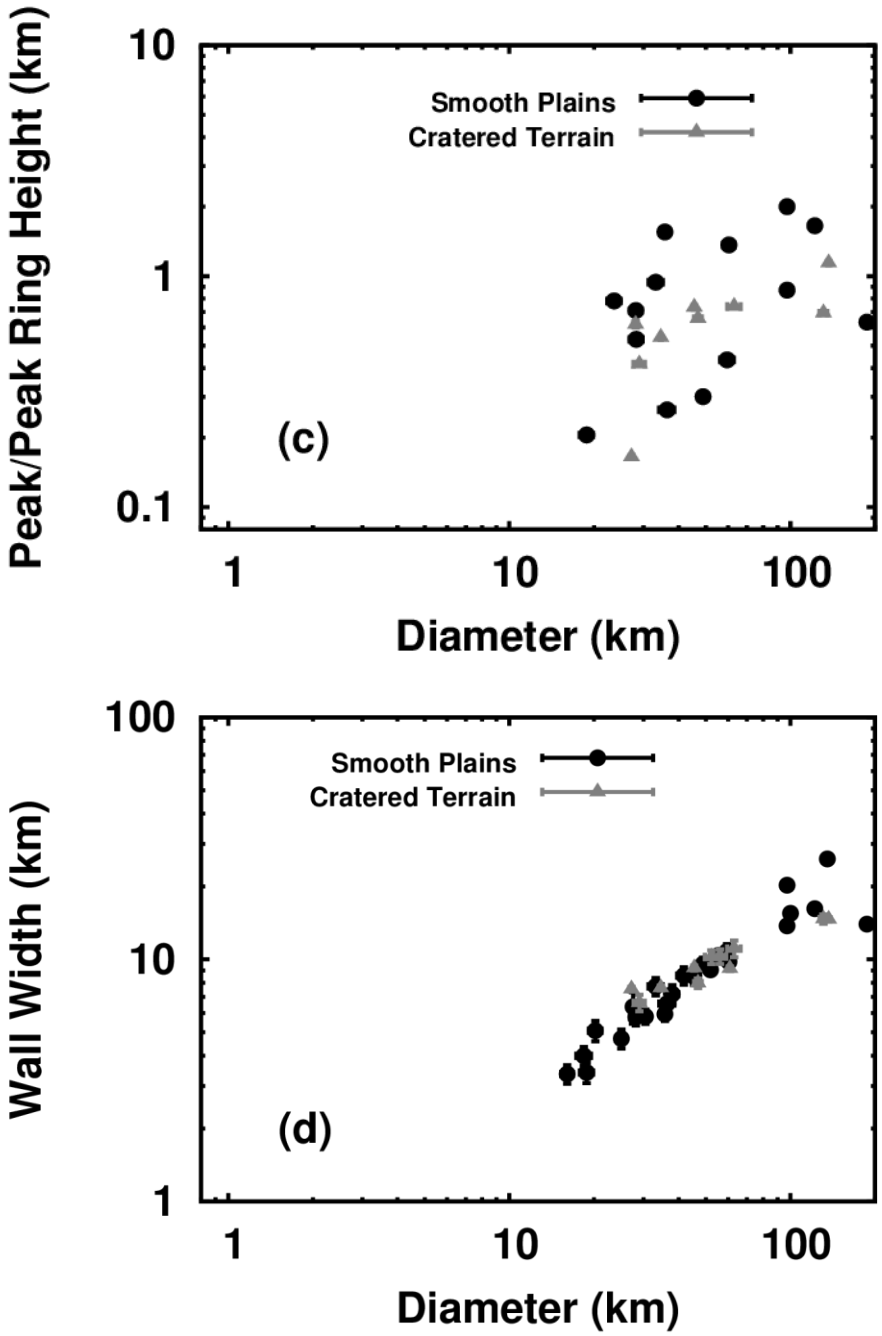

Fig. 9. (a) Relations between *d* and *D*, (b) *h* and *D*, (c) *r* and *D*, and (d) *w* and *D* for classes 4–5 craters in smooth plains versus cratered terrain.

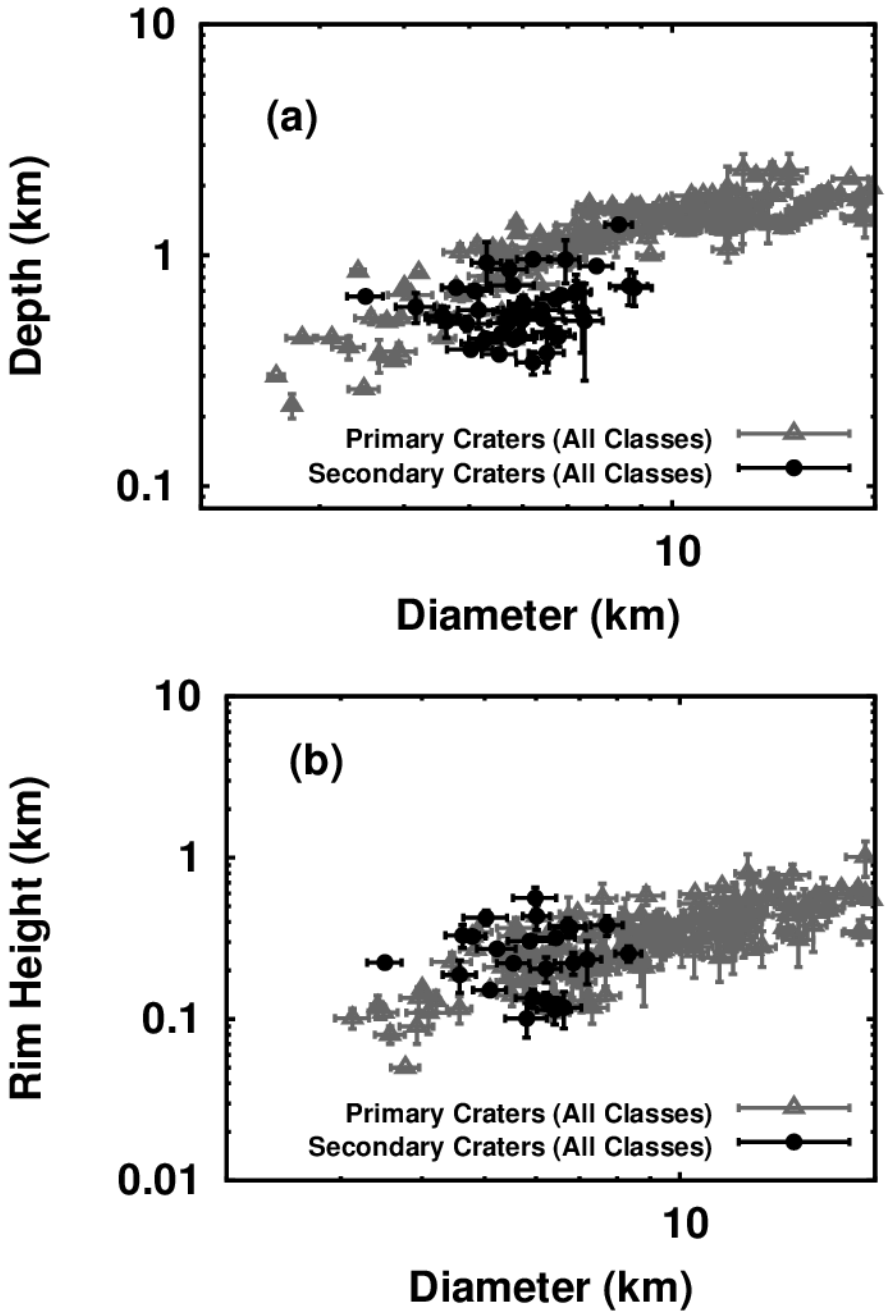

Fig. 10. (a) Relations between depth and diameter for primary versus secondary craters (all classes). Secondary craters are generally shallower, but the two populations overlap. (b) Relations between rim height and diameter for primary versus secondary craters (all classes).

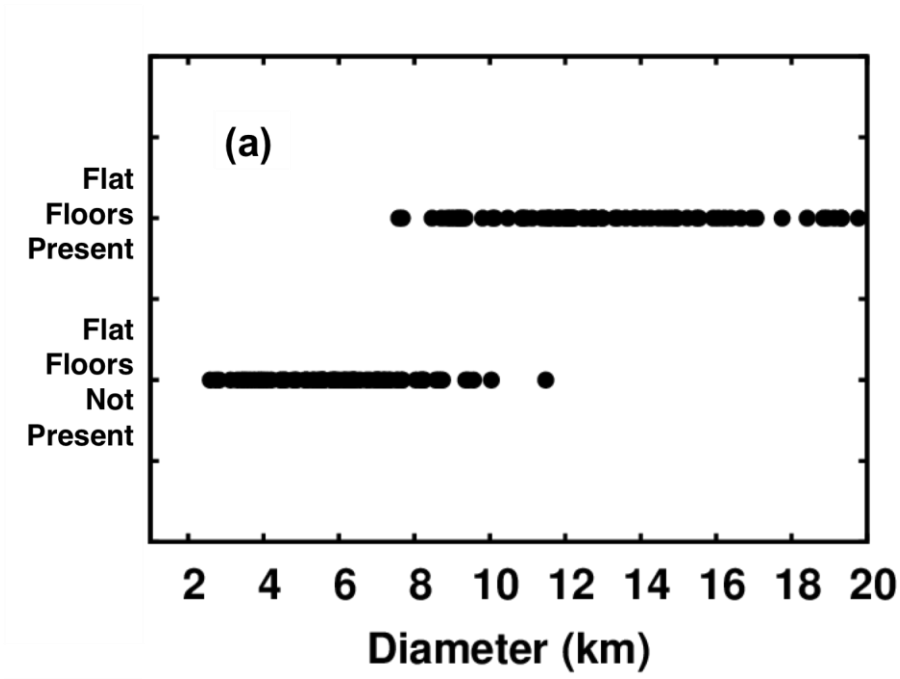
(a)
Flat Floors Present
Flat Floors Not Present
2 4 6 8 10 12 14 16 18 20
Diameter (km)

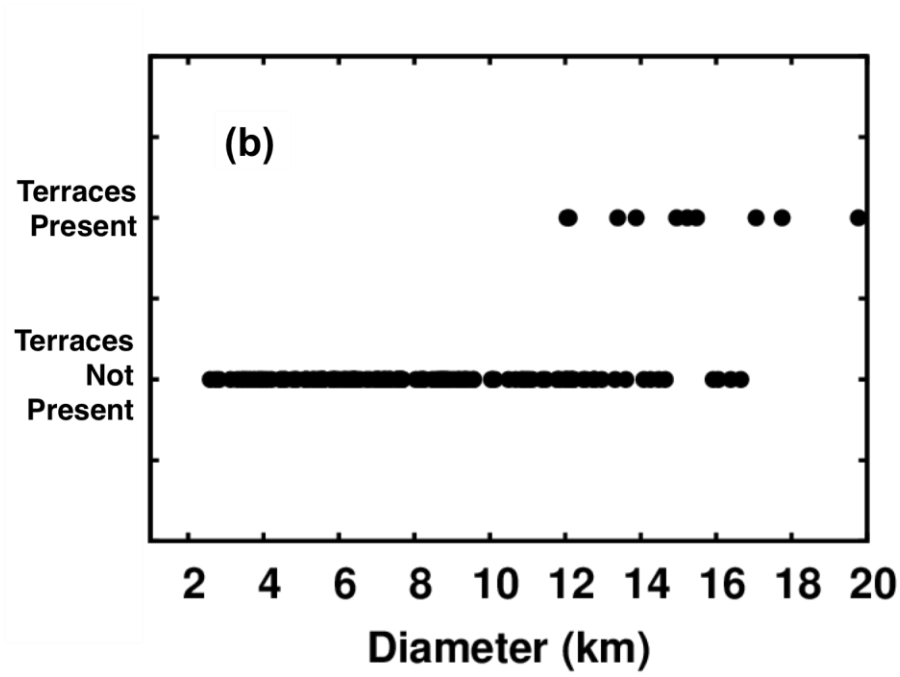
(b)
Terraces Present
Terraces Not Present
2 4 6 8 10 12 14 16 18 20
Diameter (km)

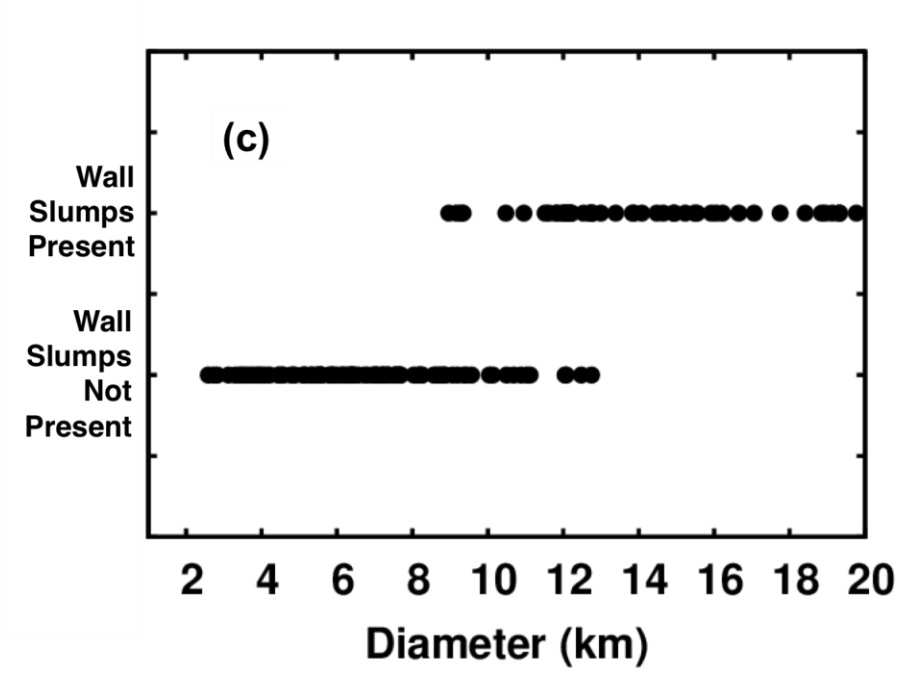

Fig. 11. The presence or absence of (a) flat floors, (b) terraces, and (c) wall slumps in craters of diameter less than 20 km, evaluated from both MLA profiles and MDIS images. The median diameter of overlap between "present" and "not present" was used to calculate the D_t value for Mercury.

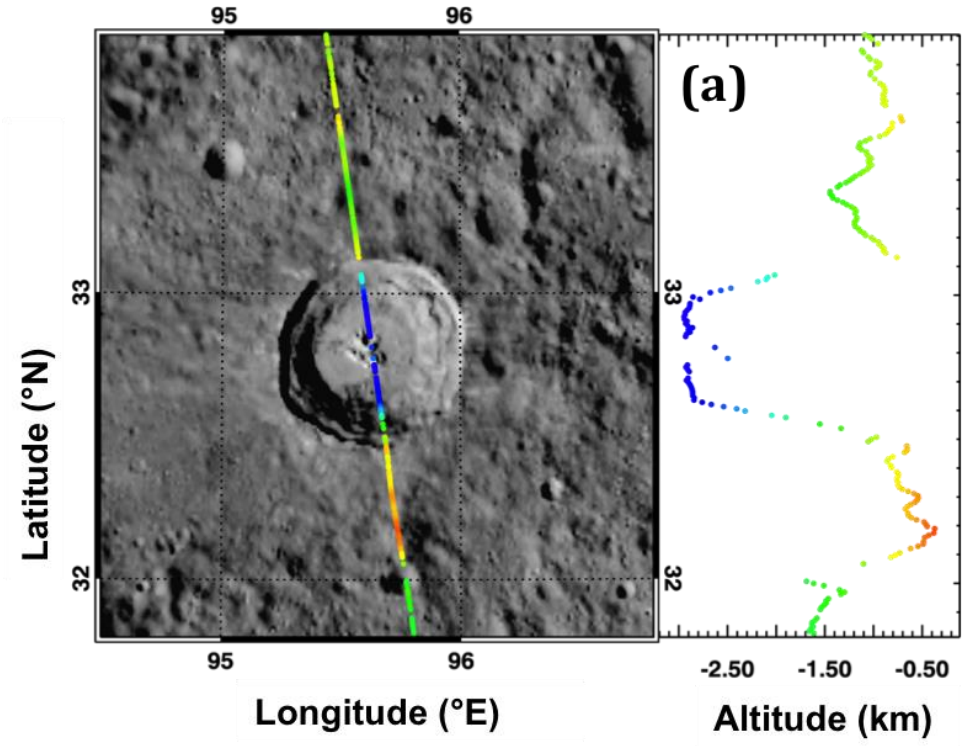
95
96
(a)
33
32
Latitude (°N)
95
96
Longitude (°E)
-2.50
-1.50
-0.50
Altitude (km)

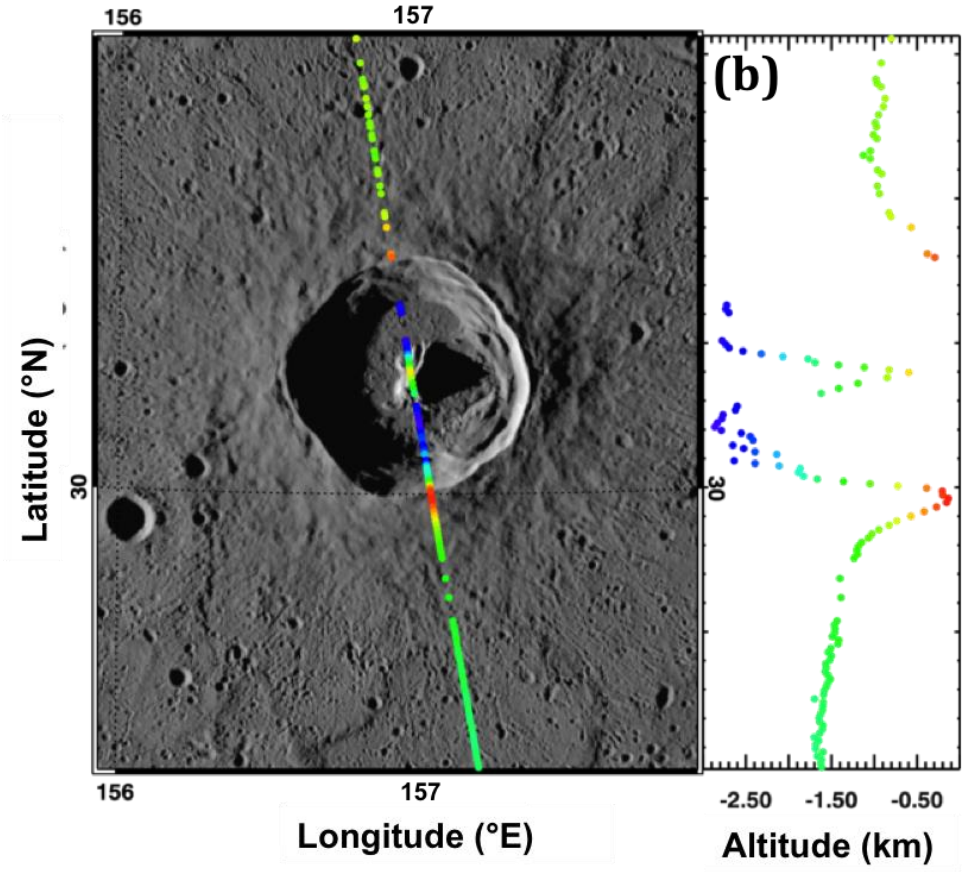
156
157
(b)
30
Latitude (°N)
156
157
Longitude (°E)
-2.50
-1.50
-0.50
Altitude (km)

Fig. 12. The craters (a) Fonteyn (32.85ºN, 95.67ºE) and (b) Cunningham (30.40ºN, 157.18ºE), both fresh, class-5 craters. Fonteyn, found in cratered terrain (D= 29.0 ± 1.3; d= 2.3 ± 0.2), is deeper than Cunningham (D= 35.8 ± 0.5; d= 1.9 ± 0.1), which formed in smooth plains.

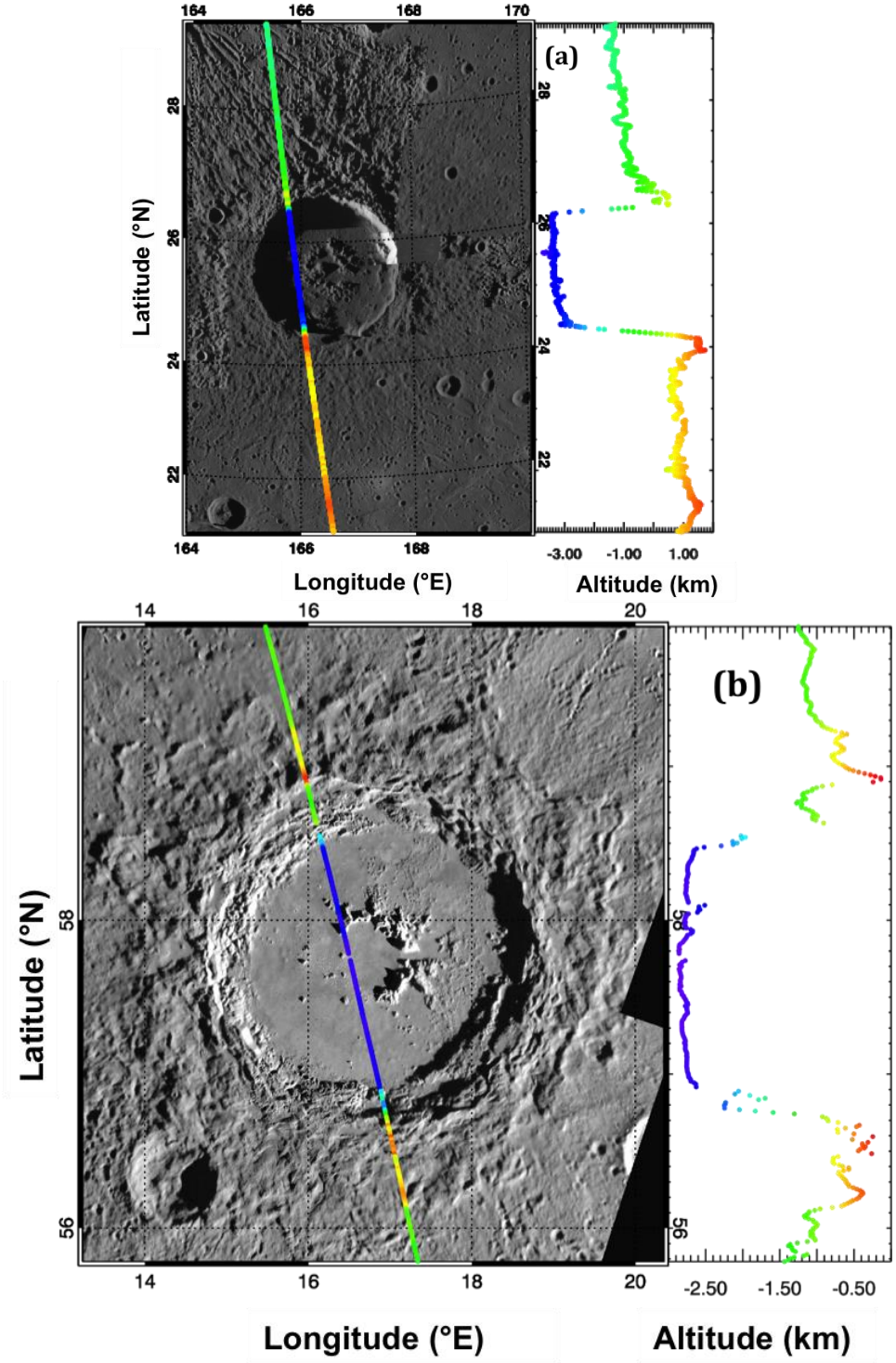

Fig. 13. The craters (a) Atget (25.6ºN, 166.42ºE; D = 102 ± 1.1 km; d = 3.2 ± 0.5 km; class 4) and (b) Hokusai (57.69ºN, 16.87ºE ; D = 97.3 ± 1.1 km; d = 2.3 ± 0.2 km; class 5), both craters within smooth plains units. The difference in topography on either side of Atget (a) was corrected before the crater depth was measured (see Section *3.1.1* for more information).

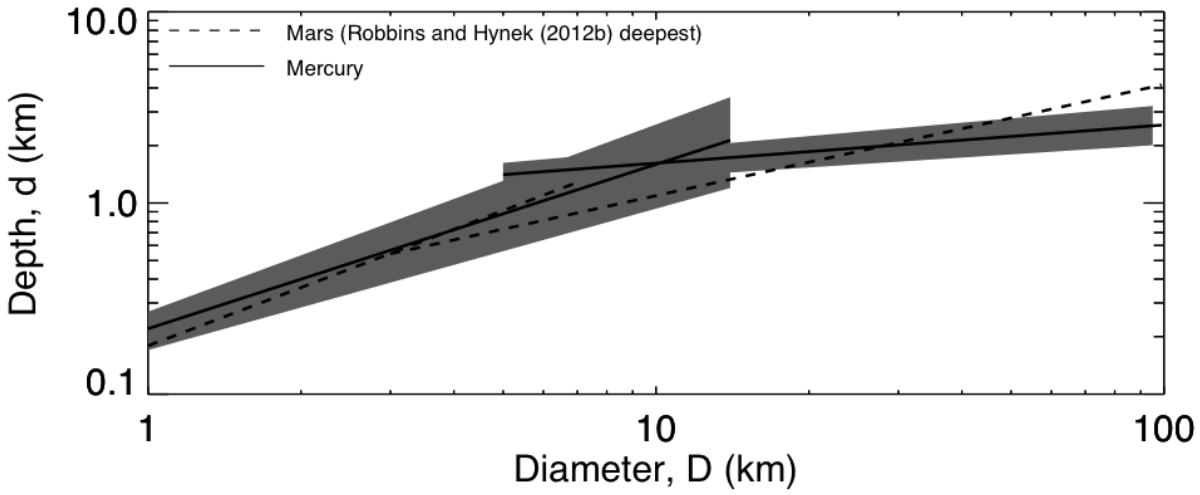

Fig. 14. Power laws fit to values of *d* versus *D* on Mercury and Mars. The power laws for craters on Mars (dashed lines) are from Robbins and Hynek (2012b). The power laws for craters on Mercury (solid lines) are from this study (see Table 1). The gray region represents the standard error on the Mercury power-law fits.

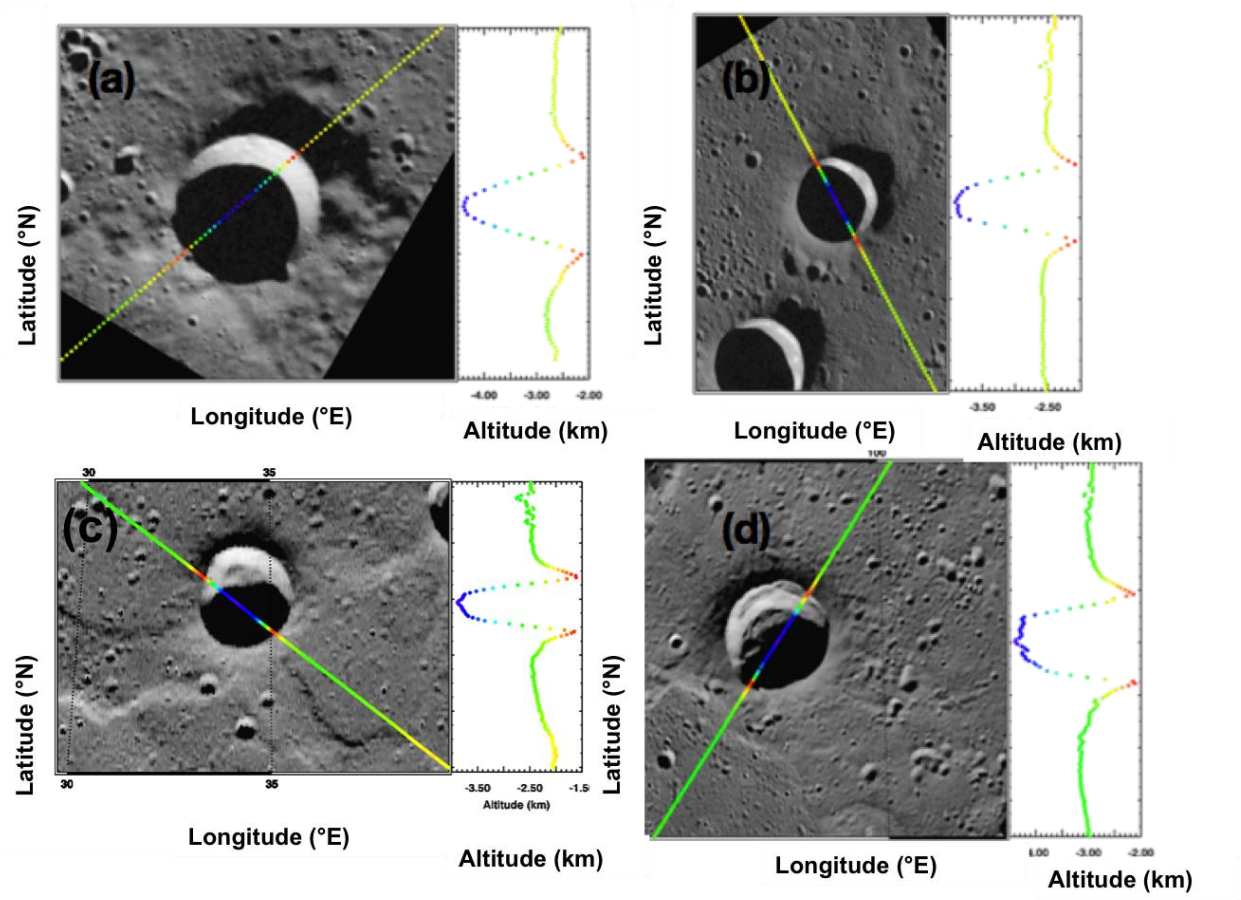

Fig. 15. Examples of craters with the morphologies used to identify the diameter of the onset of complex craters: (a) 503 (81.53ºN, 129.19ºE; *D* = 10.7 ± 0.7 km), a bowl-shaped crater. (b) 440 (76.20ºN, 135.35ºE; *D* = 8.7 ± 0.7 km), a flat-floored crater. (c) 499 (81.84ºN, 34.19ºE; *D* = 15.9 ± 1.1 km), exhibiting wall collapse. (d) 1037 (78.42ºN, 97.96ºE; *D* = 18.9 ± 0.7), exhibiting terracing.

Table 1. Power laws fit to crater depth versus diameter from this work and earlier studies.

	MESSENGER orbital data (this study)	MESSENGER flyby data (Barnouin et al., 2012)	MESSENGER orbital data (Talpe et al., 2012)	Mariner 10 flyby images (Pike, 1988)[1]
Simple, classes 4 and 5 (5–10 km diameter)	$d = (0.22 \pm 0.05)D^{(0.86 \pm 0.12)}$	$d = (0.18 \pm 0.10)D^{(0.98 \pm 0.04)}$	NA	$d = 0.199D^{0.995}$
Complex, classes 4 and 5	$d = (1.02 \pm 0.10)D^{(0.20 \pm 0.03)}$	NA	NA	$d = 0.492D^{0.418}$
All simple	$d = (0.17 \pm 0.04)D^{(0.96 \pm 0.11)}$	$d = (0.18 \pm 0.10)D^{(0.98 \pm 0.04)}$	$d = 0.138D^{0.970}$	NA
All complex	$d = (0.89 \pm 0..06)D^{(0.24 \pm 0.02)}$	NA	$d = 0.77D^{0.24}$	NA

[1]Pike (1988) did not distinguish craters on the basis of the Trask (1971) morphological classification, but instead measured only "fresh craters," which appear to correspond to classes 4 and 5.

Table 2. Power laws fit to crater rim height versus diameter from this work and earlier studies.

	MESSENGER orbital data (this study)	Mariner 10 flyby images (Pike, 1988)
Simple, classes 4 and 5 (5–10 km)	$h = (0.02 \pm 0.02)D^{(1.32 \pm 0.43)}$	$h = 0.052D^{0.930}$
Complex, classes 4 and 5	$h = (0.31 \pm 0.09)D^{(0.21 \pm 0.07)}$	$h = 0.150D^{0.487}$
All simple	$h = (0.02 \pm 0.01)D^{(1.19 \pm 0.32)}$	NA
All complex	$h = (0.25 \pm 0.06)D^{(0.28 \pm 0.06)}$	NA

Table 3. Power laws fit to crater wall width versus diameter from this work.

	MESSENGER orbital data (this study)
Complex, classes 4 and 5	$w = (1.65 \pm 0.50)D^{(0.47 \pm 0.08)}$
All complex	$w = (0.92 \pm 0.30)D^{(0.62 \pm 0.07)}$

Table 4. Transition diameter (D_t) from simple to complex crater obtained for each morphologic attribute.

Morphologic attribute	Statistic	Diameter (km)
d versus *D*		10.2
	Intersection of fits	
h versus *D*		13.0
	Intersection of fits	
		10.1
Complex crater	Smallest complex crater	
Simple crater	Largest simple crater	16.4
	Median *D* of overlap[1]	
Terraces		14.4
Flat floor	Median *D* of overlap[1]	9.6
	Median *D* of overlap[1]	
Wall slump		10.3
Final D_t	Geometric mean	**11.7 ± 1.2**

[1]The median of the diameters of craters in the diameter interval containing both craters with a terrace (or flat floor, or wall slump) and craters without.